

Loss of FLCN-FNIP1/2 induces a non-canonical interferon response in human renal tubular epithelial cells

Iris E Glykofridis^{1*}, Jaco C Knol², Jesper A Balk¹, Denise Westland³, Thang V Pham², Sander R Piersma², Sinéad M Loughheed², Sepide Derakhshan⁴, Puck Veen¹, Martin A Roimans¹, Saskia E van Mil¹, Franziska Böttger², Pino J Poddighe⁵, Irma van de Beek⁵, Jarno Drost⁴, Fried JT Zwartkruis³, Renee X de Menezes⁶, Hanne EJ Meijers-Heijboer¹, Arjan C Houweling⁵, Connie R Jimenez^{2*}, Rob MF Wolthuis^{1*}

¹Amsterdam UMC, location VUmc, Vrije Universiteit Amsterdam, Clinical Genetics, Cancer Center Amsterdam, Amsterdam, Netherlands; ²Amsterdam UMC, location VUmc, Vrije Universiteit Amsterdam, Medical Oncology, Cancer Center Amsterdam, Amsterdam, Netherlands; ³University Medical Center Utrecht, Center for Molecular Medicine, Molecular Cancer Research, Universiteitsweg, Utrecht, Netherlands; ⁴Princess Máxima Center for Pediatric Oncology, Oncode Institute, Heidelberglaan, Utrecht, Netherlands; ⁵Amsterdam UMC, location VUmc, Vrije Universiteit Amsterdam, Clinical Genetics, Amsterdam, Netherlands; ⁶NKI-AvL, Biostatistics Unit, Amsterdam, Netherlands

***For correspondence:**

i.glykofridis@amsterdamumc.nl (IEG);

c.jimenez@amsterdamumc.nl (CRJ);

r.wolthuis@amsterdamumc.nl (RMFW)

Competing interests: The authors declare that no competing interests exist.

Funding: See page 25

Received: 31 July 2020

Accepted: 16 January 2021

Published: 18 January 2021

Reviewing editor: Wilbert Zwart, Netherlands Cancer Institute, Netherlands

© Copyright Glykofridis et al. This article is distributed under the terms of the [Creative Commons Attribution License](https://creativecommons.org/licenses/by/4.0/), which permits unrestricted use and redistribution provided that the original author and source are credited.

Abstract Germline mutations in the Folliculin (*FLCN*) tumor suppressor gene cause Birt–Hogg–Dubé (BHD) syndrome, a rare autosomal dominant disorder predisposing carriers to kidney tumors. *FLCN* is a conserved, essential gene linked to diverse cellular processes but the mechanism by which *FLCN* prevents kidney cancer remains unknown. Here, we show that disrupting *FLCN* in human renal tubular epithelial cells (RPTEC/TERT1) activates TFE3, upregulating expression of its E-box targets, including RRAGD and GPNMB, without modifying mTORC1 activity. Surprisingly, the absence of *FLCN* or its binding partners FNIP1/FNIP2 induces interferon response genes independently of interferon. Mechanistically, *FLCN* loss promotes STAT2 recruitment to chromatin and slows cellular proliferation. Our integrated analysis identifies STAT1/2 signaling as a novel target of *FLCN* in renal cells and BHD tumors. STAT1/2 activation appears to counterbalance TFE3-directed hyper-proliferation and may influence immune responses. These findings shed light on unique roles of *FLCN* in human renal tumorigenesis and pinpoint candidate prognostic biomarkers.

Introduction

Renal cell carcinoma (RCC) is the most common form of kidney cancer representing up to 5% of newly identified cancer cases (Ferlay et al., 2019; Lopez-Beltran et al., 2006; Siegel et al., 2018). Generally, RCCs are diagnosed in adults, with the exception of translocation RCC, which is driven by a hyper-activated fusion protein of the transcriptional activators TFE3 or TFEB and comprises 20–75% of RCCs in childhood (Ambalavanan and Geller, 2019; Caliò et al., 2019; Lee et al., 2018). Birt-Hogg-Dubé syndrome (BHD) is a dominantly inherited kidney cancer syndrome caused by mono-allelic germline loss-of-function mutations of the essential and conserved Folliculin (*FLCN*) gene (Nahorski et al., 2011; Nickerson et al., 2002). The lifetime risk for BHD patients to develop RCC is ~10 times higher than for the unaffected population (Houweling et al., 2011;

Pavlovich et al., 2005; Toro et al., 2008; Zbar et al., 2002). BHD patients are predisposed to bilateral and multifocal renal tumors (*Nickerson et al., 2002; Schmidt et al., 2005; Zbar et al., 2002*) and dependent on surveillance by renal imaging for early detection and curative treatment prior to metastasis (*Johannesma et al., 2019*). Loss of heterozygosity, by gene silencing or an inactivating somatic mutation of the wild-type *FLCN* allele, is a prerequisite for kidney cancer development in BHD patients (*Vocke et al., 2005*).

Much of our understanding of BHD-related RCC is based on studies in BHD animal models (*Chen et al., 2008; Chen et al., 2015; Hudon et al., 2010*) and a BHD kidney tumor-derived cell line (*Yang et al., 2008*). These studies have connected *FLCN* to diverse cellular processes including mitochondrial biogenesis, stress resistance, autophagy, membrane trafficking, stem cell pluripotency, and ciliogenesis (*Baba et al., 2006; Betschinger et al., 2013; Dunlop et al., 2014; Hasumi et al., 2012; Laviolette et al., 2013; Luijten et al., 2013; Nookala et al., 2012; Possik et al., 2014*). The *FLCN* protein has been reported to affect multiple regulatory factors including mTOR, AMPK, HIF1, TGF- β , and Wnt (*Baba et al., 2006; De Zan et al., 2020; El-Houjeiri et al., 2019; Hong et al., 2010b; Khabibullin et al., 2014; Mathieu et al., 2019; Preston et al., 2011; Yan et al., 2016*). Nevertheless, the mechanism by which *FLCN* loss induces tumorigenesis is largely unknown. Conflicting results, such as activating or inhibitory effects of *FLCN* on mTOR signaling (*Baba et al., 2006; Bastola et al., 2013; Hartman et al., 2009; Hasumi et al., 2009; Hudon et al., 2010; Napolitano et al., 2020; Takagi et al., 2008; Tsun et al., 2013*), and the range of the processes attributed to *FLCN* loss, prohibit a clear understanding of the pathways by which *FLCN* suppresses renal tumorigenesis.

Here, we present the molecular and cellular consequences of knocking out *FLCN* or its binding partners *FNIP1/FNIP2* in a human renal proximal tubular epithelial cell model, representing the cells of origin of RCC (*Holthöfer et al., 1983*). We performed RNA sequencing (RNAseq) and proteomics, followed by pathway analyses and mining of regulatory promotor motifs of differentially expressed genes, revealing that *FLCN* loss induces two separate transcriptional signatures. The first is characterized by E-box controlled genes and confirms TFE3 as a main target of the *FLCN-FNIP1/2* axis (*El-Houjeiri et al., 2019; Endoh et al., 2020; Hong et al., 2010b; Petit et al., 2013*). Secondly, we discovered that loss of *FLCN-FNIP1/2* induces a set of genes under control of interferon-stimulated response elements (ISREs). The ISRE gene activation program is directed by upregulate STAT1 and STAT2 and may explain why loss of the *FLCN* tumor suppressor, paradoxically, reduces cellular proliferation. We propose that TFE3 and STAT1/2 are the two main, independent transcriptional effectors of *FLCN-FNIP1/2* loss in human renal epithelial cells. Preliminary data indicate that these gene networks may also be activated in BHD tumors. Taken together, our findings may help the development of prognostic biomarkers or targeted therapies.

Results

Knocking out *FLCN* activates TFE3 in renal proximal tubular cells

To study the effects of *FLCN* loss in a context relevant for oncogenesis, we used an immortalized, diploid renal proximal tubular epithelial cell line (RPTEC/TERT1, ATCC CRL-4031; *Wieser et al., 2008*, hereafter called RPTEC) as a model system, which retains the capacity to form 3D tubular structures (*Figure 1A*). First, we constructed an inducible Cas9-expressing RPTEC cell line and verified doxycycline-induced Cas9 protein expression by immunoblots (*Figure 1B*). Because a TP53-dependent DNA damage response prohibits effective gene editing in some cell types (*Haapaniemi et al., 2018; Ihry et al., 2018*), we simultaneously knocked-out *TP53* and *FLCN* to improve targeting efficiency. Guide RNAs (gRNAs) targeting 5' coding exons of *TP53* and *FLCN* (*Figure 1C*) were co-transfected and targeted exons of single-cell derived clones were sequenced. *Indel* analysis showed that each clone carried a unique genetic disruption of *FLCN* and *TP53* (*Figure 1—figure supplement 1A*). By karyotypic analysis, we found that four out of six knock out (KO) cell lines had become aneuploid (*Figure 1D*). We conclude, however, that aneuploidy occurred spontaneously during cell line formation because it appeared independently of *FLCN*, *TP53*, or inducible Cas9 status (*Figure 1D*). At a later stage, we indeed developed diploid *FLCN* knock out RPTEC cell lines using more advanced gRNA delivery assays (see below). However, considering that kidney tumors are often aneuploid (*Kardas et al., 2005; Morlote et al., 2019*), we first used the cell

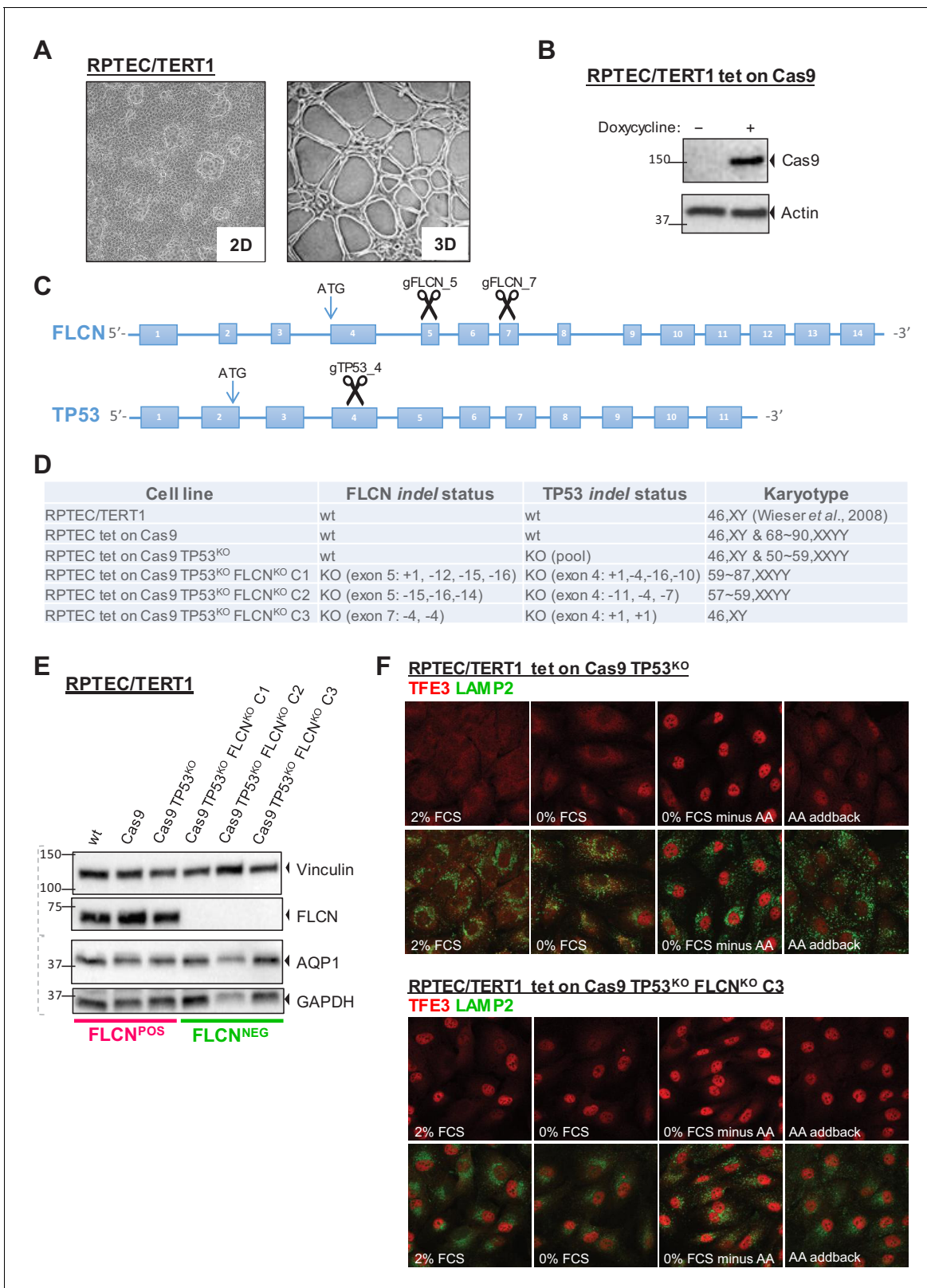


Figure 1. Renal proximal tubular epithelial cells as a model for FLCN loss. (A) Brightfield images ($\times 50$ magnification) of a human renal proximal tubular epithelial cell model (RPTEC/TERT1). Left image shows 2D culture of cells with typical dome formation. Right image shows 3D tubular structures that form when RPTECs are cultured according to *Secker, 2018*. (B) Doxycycline-inducible Cas9 expression of RPTEC tet-on Cas9 cell line. Cas9 protein expression after 24 hr treatment with 10 ng/ml doxycycline was assessed by immunoblotting. Experiment was performed twice. (C) CRISPR/Cas9-
 Figure 1 continued on next page

Figure 1 continued

mediated knockout strategy of FLCN and TP53 in RPTEC/TERT1 cells; gRNAs were designed to target early exons of FLCN and TP53 coding regions. (D) Overview of FLCN and TP53 *indel* status and karyotype per selected cell line clone. Cell-line-specific Sanger sequence chromatograms are shown in **Figure 1—figure supplement 1A**. (E) Western blot of FLCN protein levels of indicated cell line clones. Expression of renal proximal tubular-specific marker AQP1 is shown as a control. Dotted lines indicate separate blots. Western blot of TP53 protein levels is shown in **Figure 1—figure supplement 1B**. (F) Immunofluorescence staining of TFE3 and lysosomal marker LAMP2 show enhanced nuclear TFE3 upon FLCN loss independent of nutrient availability. FCS = fetal calf serum, AA = amino acids. Staining of FLCN^{KO} RPTEC C1 and C2 are shown in **Figure 1—figure supplement 1C**. The online version of this article includes the following figure supplement(s) for figure 1:

Figure supplement 1. Characterization of TP53^{KO} and FLCN^{KO} cell lines.

lines of **Figure 1D** to identify FLCN-specific effects that occur independently of karyotype. We started by comparing two groups of cell lines: RPTEC ('WT'), RPTEC tet-on Cas9 ('Cas9'), and RPTEC tet-on Cas9 TP53^{-/-} ('TP53^{KO}') were assigned to the FLCN^{POS} group, while three individually isolated RPTEC tet-on Cas9 TP53^{-/-} FLCN^{-/-} clones ('FLCN^{KO} C1', 'FLCN^{KO} C2', and 'FLCN^{KO} C3') were assigned to the FLCN^{NEG} group. C1 and C2 were created by gRNAs targeting FLCN exon 5 ('gFLCN_5') and C3 by gRNAs targeting FLCN exon 7 ('gFLCN_7'). Loss of FLCN and TP53 protein expression was confirmed by immunoblots, which also showed that expression of the renal proximal tubular marker aquaporin-1 (AQP1) was unchanged (*Bedford et al., 2003; Figure 1E and Figure 1—figure supplement 1B*).

Previous studies reported that FLCN prevents nuclear localization of TFE3 under nutrient-rich conditions. TFE3, and its close family member TFEB, are transcription factors directing an autophagy and stress tolerance gene program under growth restrictive conditions (*Hong et al., 2010a; Wada et al., 2016*). To investigate the status of this pathway in our FLCN knock-out RPTEC cell models, we visualized TFE3 localization in the presence or absence of FLCN. Immunofluorescence co-staining of TFE3 and the lysosomal marker LAMP2 in either fed, starved, or amino acid (AA)-depleted conditions are shown in **Figure 1F** and **Figure 1—figure supplement 1C**. RPTEC cells showed cytoplasmic TFE3 under normal growth conditions but TFE3 completely translocated to the nucleus after withdrawal of serum and amino acids (**Figure 1F**, upper panels). In contrast, TFE3 localized in the nucleus of the majority of cells from each of the three RPTEC FLCN^{NEG} cell lines, independent of starvation or refeeding, revealing that FLCN^{NEG} cells fail to convey proper nutrient sensing and TFE3 responses (**Figure 1F**, lower panels and **Figure 1—figure supplement 1C**). We conclude that, in the absence of FLCN, TFE3 is constitutively active in renal epithelial cells, confirming TFE3 as a bona fide target of the FLCN tumor suppressor (*El-Houjeiri et al., 2019; Wada et al., 2016*).

Overlapping transcriptomic and proteomic alterations induced by FLCN loss

Subsequently, we determined changes in gene transcription and protein expression patterns in our FLCN^{POS} and FLCN^{NEG} RPTEC cell lines by mRNA sequencing (RNAseq) and proteomic workflows shown in **Figure 2A**. For specificity, we only compared profiles of the FLCN^{POS} and FLCN^{NEG} cell lines between the groups defined by rectangles in **Figure 2—figure supplement 1A** (for RNAseq) and **Figure 2—figure supplement 2A** (for proteomics). To correct for possible clonal effects on global transcription, three different TP53 knock-out clones were included in the RNAseq analysis. We used edgeR (*Robinson et al., 2010*) to identify FLCN-related effects and visualized differential expressed genes in volcano plots (**Figure 2B**). Green circles show genes upregulated in FLCN^{NEG} cells and pink circles indicate genes expressed at a higher level in control (FLCN^{POS}) cells. The threshold line represents a false discovery rate (FDR) of <0.05. The edgeR results of RPTEC FLCN^{POS} versus FLCN^{NEG} comparison are in **Supplementary file 1** and a volcano plot with annotated gene names is shown in **Figure 3—figure supplement 1A**. Interestingly, the majority of significantly altered genes was induced, rather than repressed, by FLCN inactivation: in FLCN^{NEG} cells 426 genes were upregulated at least tenfold while only 62 genes were downregulated to the same extent (FDR < 0.05, **Figure 2—figure supplement 1D**, lower panel). To explore downstream consequences of FLCN loss at the protein level, we used mass spectrometry-based proteomics, identifying 5755 different proteins (**Figure 2—figure supplement 2C and E**). Comparative analysis of FLCN^{POS} versus

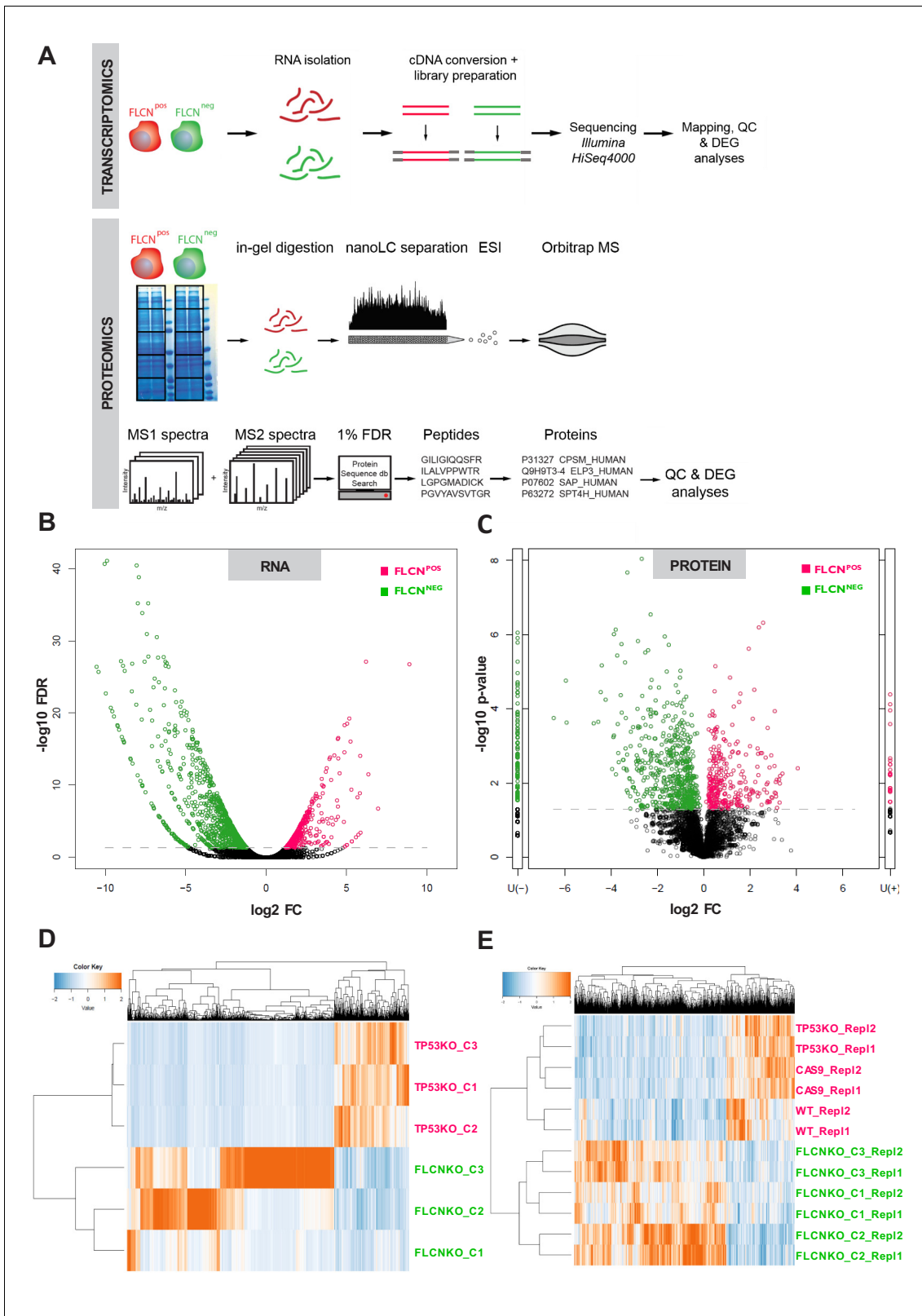


Figure 2. Integrated transcriptomic and proteomic analyses of renal tubular FLCN loss. (A) Schematic overview of transcriptomic and proteomic workflows. (B) Volcano plot showing significantly increased or decreased expression of genes in FLCN^{POS} vs. FLCN^{NEG} comparison derived from transcriptomic analysis. Colored circles above threshold line are FDR < 0.05; statistical details can be found in Materials and methods section. (C) Volcano plot showing (significantly) increased or decreased expression of proteins in FLCN^{POS} vs. FLCN^{NEG} comparison derived from proteomic analysis. (D) Heatmap showing gene expression patterns across different FLCN knock-out (KO) and knock-out control (KNO) samples. (E) Heatmap showing gene expression patterns across different FLCN knock-out (KO) and knock-out control (KNO) samples. *Figure 2 continued on next page*

Figure 2 continued

analysis. Colored circles above threshold line are $p < 0.05$. U(-) column shows proteins uniquely detected in FLCN^{NEG}, U(+) column shows proteins uniquely detected in FLCN^{POS}. Statistical details can be found in the Materials and methods section. (D) Hierarchical clustering based on FLCN-dependent differential mRNA expression. (E) Hierarchical clustering based on FLCN-dependent differential protein expression. The online version of this article includes the following figure supplement(s) for figure 2:

Figure supplement 1. Comparative analyses of RPTEC FLCN^{POS} vs. FLCN^{NEG} cell line pairs.

Figure supplement 2. GeLC-MS/MS-based proteomics of RPTEC FLCN^{POS} vs. FLCN^{NEG} cell line pairs.

FLCN^{NEG} cells using normalized spectral counts (beta-binomial test, [Pham et al., 2010]), identified the differential expression pattern presented in **Figure 2C** (threshold line indicates p -values of < 0.05). The U(-), and U(+), columns next to the volcano plots show proteins that were detected in only one of the conditions. Volcano plots annotated with corresponding protein names in are shown in **Figure 3—figure supplement 1A** and the complete comparative analysis can be found in **Supplementary file 1**.

In concordance with our RNAseq data, FLCN loss predominantly induced protein expression: 209 proteins were expressed at least fivefold higher in FLCN^{NEG} cells, versus 41 proteins that were similarly downregulated, out of a total of 914 differentially expressed proteins ($p < 0.05$ and average count > 1.5 ; **Figure 2—figure supplement 2E**, lower right). Conversely, as a control, deletion of the transcriptional activator TP53 alone (Farmer et al., 1992; Fields and Jang, 1990; Vogelstein and Kinzler, 1992) resulted in downregulation of gene expression (**Figure 2—figure supplement 1E**, right, volcano plots of differential expression analysis by edgeR). Expression of differential RNAs showed variation between FLCN^{NEG} RPTEC clones (**Figure 2D**, **Figure 2—figure supplement 1C**). Nevertheless, hierarchical cluster analysis of differentially expressed proteins showed that replicates clustered together with a clear separation between the two groups (**Figure 2D,E**, **Figure 2—figure supplement 2D**), pointing to clonally independent effects of FLCN loss. Taken together, these results identify FLCN as a powerful repressor of gene expression.

FLCN loss activates a specific set of TFE3 target genes in kidney epithelial cells

To determine which TFE3/TFEB (TFE) driven genes are activated by FLCN loss, we collected 248 previously reported TFE targets (Hong et al., 2010a; Martina et al., 2014; Palmieri et al., 2011; Santaguida et al., 2015) and performed *k-means* Pearson correlation clustering of our FLCN^{POS} vs. FLCN^{NEG} RPTEC RNAseq data to categorize the effects. Interestingly, we found a specific subset of 115 known TFE targets to be upregulated in all three FLCN^{NEG} cell lines (**Figure 3A**, cluster 3, boxed yellow, **Supplementary file 2**). Consistent upregulation of TFE target genes FNIP2, GPNMB, SQSTM1, RRAGC, GABARAP, ARHGAP12, AMDHD, WIPI1 and the more recently identified tumor growth-promoting TFE target RRAGD (not included in **Figure 3A**; Di Malta et al., 2017) was validated in all three FLCN^{NEG} RPTEC clones using quantitative RT-PCR (**Figure 3B**). Western blots of GPNMB, RRAGD, SQSTM1, and FNIP2, proteins associated with lysosome function, also showed these were strongly upregulated by FLCN inactivation, irrespective of TP53 status (**Figure 3C**; TP53^{wt} FLCN^{KO} refers to a TP53 positive FLCN knock out clone, see **Figure 3—figure supplement 1B**). Induction of GPNMB, RRAGD, SQSTM1, FNIP2 and other E-box targets was significantly ameliorated in all three FLCN^{NEG} RPTEC clones by simultaneously knocking down TFE3 and its close family member TFEB (**Figure 3D**; siTFE3 only is shown in **Figure 3—figure supplement 1C**), an effect further confirmed in a TP53^{wt} FLCN^{KO} cell line shown in **Figure 8—figure supplement 1C**. We conclude that FLCN loss activates a specific category of TFE target genes in renal epithelial cells, independent of TP53 or karyotype, many of which function in autophagy and lysosome regulation.

Since the nutrient-sensing capabilities of mTOR had been associated with both FLCN and TFE3 activity in previous studies (Baba et al., 2006; Bastola et al., 2013; El-Houjeiri et al., 2019; Hasumi et al., 2009; Hong et al., 2010b; Hudon et al., 2010; Petit et al., 2013; Takagi et al., 2008), we next assessed FLCN-dependent changes in canonical mTOR signaling. However, phosphorylation levels of two direct mTORC1 targets, 4E-BP1 (as judged by its electrophoretic mobility shift) and S6 kinase (S6K_T389) were not changed by FLCN loss in RPTECs, while also AKT/PKB_S437 phosphorylation remained intact (**Figure 4A**). The dynamic subcellular localization of

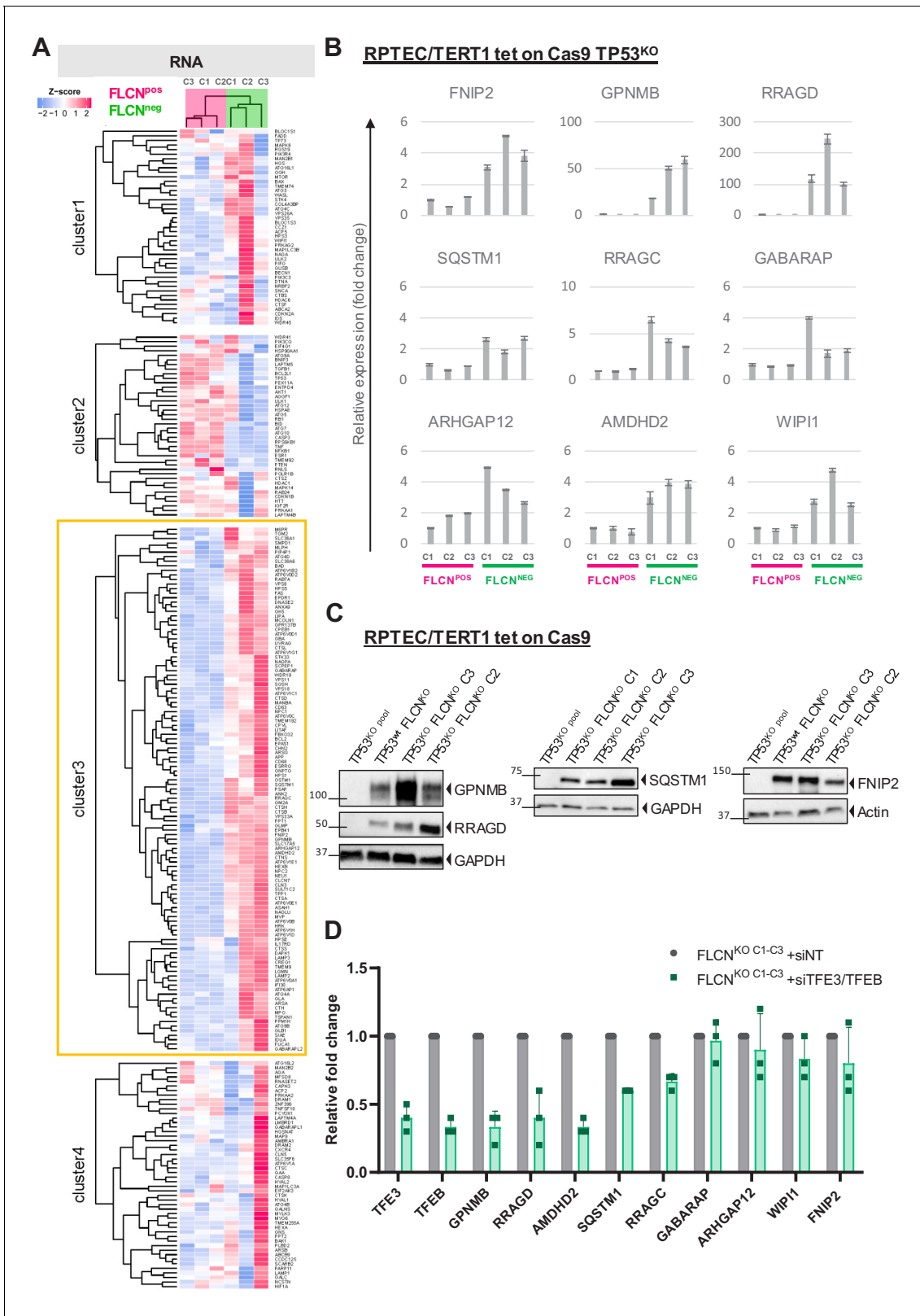


Figure 3. FLCN loss results in upregulation of subset of TFE target genes. (A) Heat map showing k-means Pearson correlation clustering of TMM-normalized RNAseq data of FLCN^{POS} versus FLCN^{NEG} RPTECs. We analyzed published TFE3/TFEB target genes. Yellow boxed cluster three shows the subset (n = 115) of TFE3/TFEB targets upregulated in all three FLCN^{NEG} clones. (B) Upregulation of TFE target genes FNIP2, GPNMB, RRAGD, SQSTM1, RRAGC, GABARAP, ARHGAP12, AMDHD2, and WIP11 in FLCN^{NEG} RPTECs. Results of three independent experiments with three technical replicates. (C) Western blots showing protein levels of TFE target genes in TP53^{KO} and TP53^{KO} FLCN^{KO} clones. GAPDH and Actin are loading controls. (D) Bar graph showing relative fold change of TFE target genes in FLCN^{KO} cells treated with siNT or siTFE3/TFEB. Error bars represent standard deviation.

Figure 3 continued

replicates. To determine quantitative gene expression levels, data were normalized to the geometric mean of two housekeeping genes. See **Figure 3—source data 1** for raw qRT-PCR values and fold change calculations. (C) Western blots of RPTEC/TERT1 tet-on Cas9 cell lines. All FLCN^{NEG} clones show strong induction of protein expression of TFE targets GPNMB, RRAGD, SQSTM1, and FNIP2. GAPDH and Actin were used as loading controls. Western blots were performed three times. (D) Knock down of TFE3/TFEB (10 nM siRNA, 72 hr) ameliorates the TFE expression gene signature induced by FLCN loss in three FLCN^{NEG} clones. Expression levels were determined by qRT-PCR, normalized to siNT-treated clones and are representative of three independent experiments. To determine quantitative gene expression data levels were normalized to the geometric mean of two housekeeping genes. Also see **Figure 8—figure supplement 1C**. Effects of siTFE3 alone are shown in **Figure 3—figure supplement 1C**. See **Figure 3—source data 1** for raw qRT-PCR values and fold change calculations.

The online version of this article includes the following source data and figure supplement(s) for figure 3:

Source data 1. Raw qRT-PCR values and fold change calculations belonging to **Figure 3B and D** and **Figure —figure supplement 1C**.

Figure supplement 1. Comparative analyses of RPTEC FLCN^{POS} vs. FLCN^{NEG} cell line pairs and validations of TP53^{WT} FLCN^{KO} RPTEC cell line.

mTOR in response to starvation did not differ between FLCN^{POS} and FLCN^{NEG} as detected by immunofluorescent co-staining of mTOR and lysosomal marker LAMP2 (**Figure 4B**, FLCN^{NEG} C3 is representative of the three FLCN^{NEG} clones which all show normal mTOR dynamics). So, in contrast to several previous studies, but in line with a recent report (*El-Houjeiri et al., 2019*), we found no evidence for directly altered mTOR signaling or nutrient sensing in the absence of FLCN in renal tubular cells.

An interferon (IFN) gene signature is induced in the absence of FLCN

To further identify the main biological processes influenced by FLCN expression, we performed Molecular Signatures Database (MSigDB) gene set enrichment analyses (GSEA) (*Subramanian et al., 2005*) on both RNA and protein data sets (pre-ranked list of p-values, classic ES). **Figure 5A** displays hallmark gene sets ranked by normalized enrichment score (NES) and significance (FDR is represented by the size of the dot). Gene sets significantly enriched in either RNA or protein (FDR < 0.05) are shown, with biological processes enriched in FLCN^{NEG} indicated in green, and processes enriched in FLCN^{POS} in pink. An overview of less significant (FDR > 0.05) hallmark gene sets is shown in **Figure 6—figure supplement 1A**. We found a higher representation of cell cycle related processes in FLCN^{POS} cells, in both RNA and protein data (**Figure 5A**, **Figure 6—figure supplement 1A**, pink marks: E2F_TARGETS, G2M_CHECKPOINT, MITOTIC_SPINDLE, MYC_TARGETS). Growth curves confirmed that deletion of FLCN reduced proliferation of RPTEC cells significantly ($p=8.31E-11$; Table 1 and accompanying Figure in Materials and methods), an unexpected effect of tumor suppressor gene inactivation (**Figure 5B**). Other typical cellular processes and signal transduction cascades that mark FLCN^{POS} RPTECs were MTORC1_SIGNALING, HYPOXIA, and TGF_BETA_SIGNALING. Interestingly, however, in FLCN^{NEG} RPTECs, the immune-response-related hallmarks were highly significantly enriched in both RNA and protein data (**Figure 5A**, **Figure 6—figure supplement 1A**, IFN_GAMMA_RESPONSE, IFN_ALPHA_RESPONSE, COMPLEMENT). BinGO (*Maere et al., 2005*) gene ontology analyses of differential expression patterns in FLCN^{NEG} RPTECs also revealed many overlapping immune and IFN response signature genes, including ISG15, IFIT1, IF16, MX1, OAS2, and STAT2 in both RNA and protein data (**Figure 5C,D**; orange circles show overlap). These findings indicate that the IFN response signature program is a key target of FLCN in renal epithelial cells.

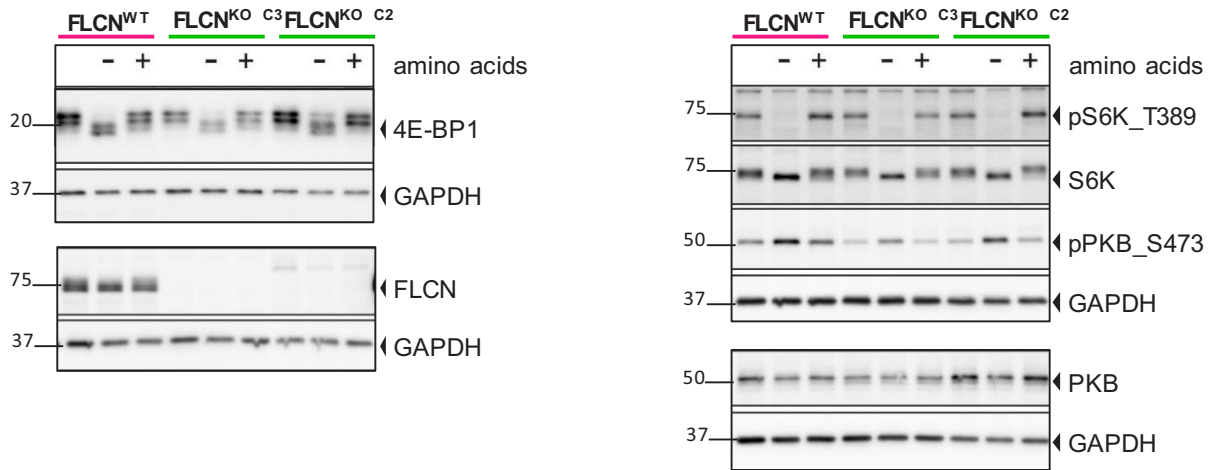
Two distinct transcriptional programs are strongly induced by FLCN loss

To specify how transcription is changed in FLCN^{NEG} RPTEC, we used iRegulon (*Janky et al., 2014*), which prioritizes candidate regulatory transcription factors based on enriched promotor motifs upstream of the transcription start sites (TSS) (**Figure 6A**). The iRegulon analysis of distinct promotor motifs directing genes upregulated in FLCN^{NEG} ($n = 711$, FDR < 0.05 and logFC > 2) are shown in **Figure 6B**. A similar overview is shown in **Figure 6C**, based on significantly upregulated proteins in FLCN^{NEG} RPTEC ($n = 498$, $p < 0.05$ and FC > 2).

Importantly, the majority of regulatory elements enriched in FLCN^{NEG} RPTEC can be assigned to either the basic helix-loop-helix E-box motif group (e.g. regulated by TFE3/TFEB) or to the Interferon-Stimulated Response Element (ISRE) motif group (**Figure 6D**). In FLCN^{POS} RPTECs, iRegulon

A

RPTEC/TERT1 tet on Cas9 TP53^{KO} - serum starved



B

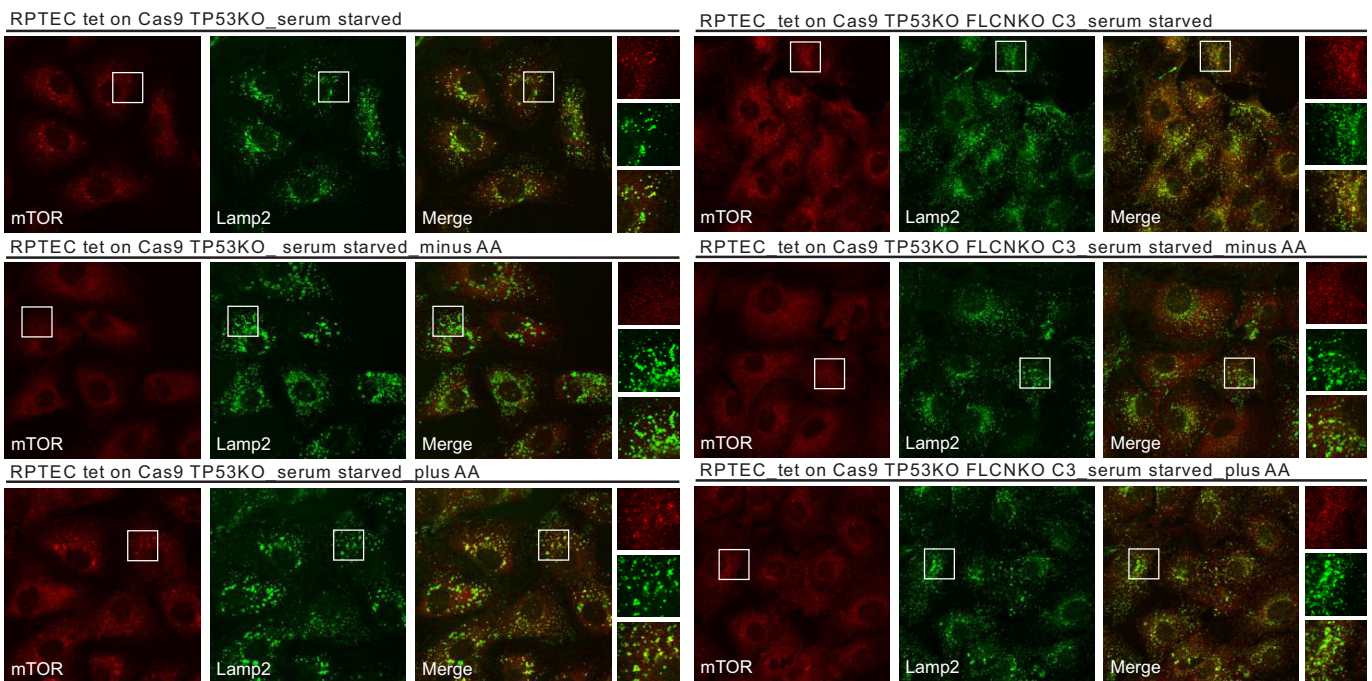


Figure 4. mTOR localization and signaling in response to starvation does not change upon FLCN loss in RPTEC. (A) To detect changes in canonical mTOR signaling, phosphorylation levels of S6 kinase (S6K_T389) and AKT/PKB (PKB_S473) and total protein levels of S6K, AKT/PKB, 4E-BP1 were assessed by western blot. Serum starved FLCN^{POS} and FLCN^{NEG} RPTEC cell lines with and without additional amino acids (AA) depletion were analyzed three times. (B) Immunofluorescence staining of mTOR and lysosomal marker LAMP2 show no FLCN dependent difference of mTOR localization in response to starvation. FCS = fetal calf serum, AA = amino acids. Staining of FLCN^{NEG} RPTEC C3 is representative for three independent FLCN^{NEG} clones.

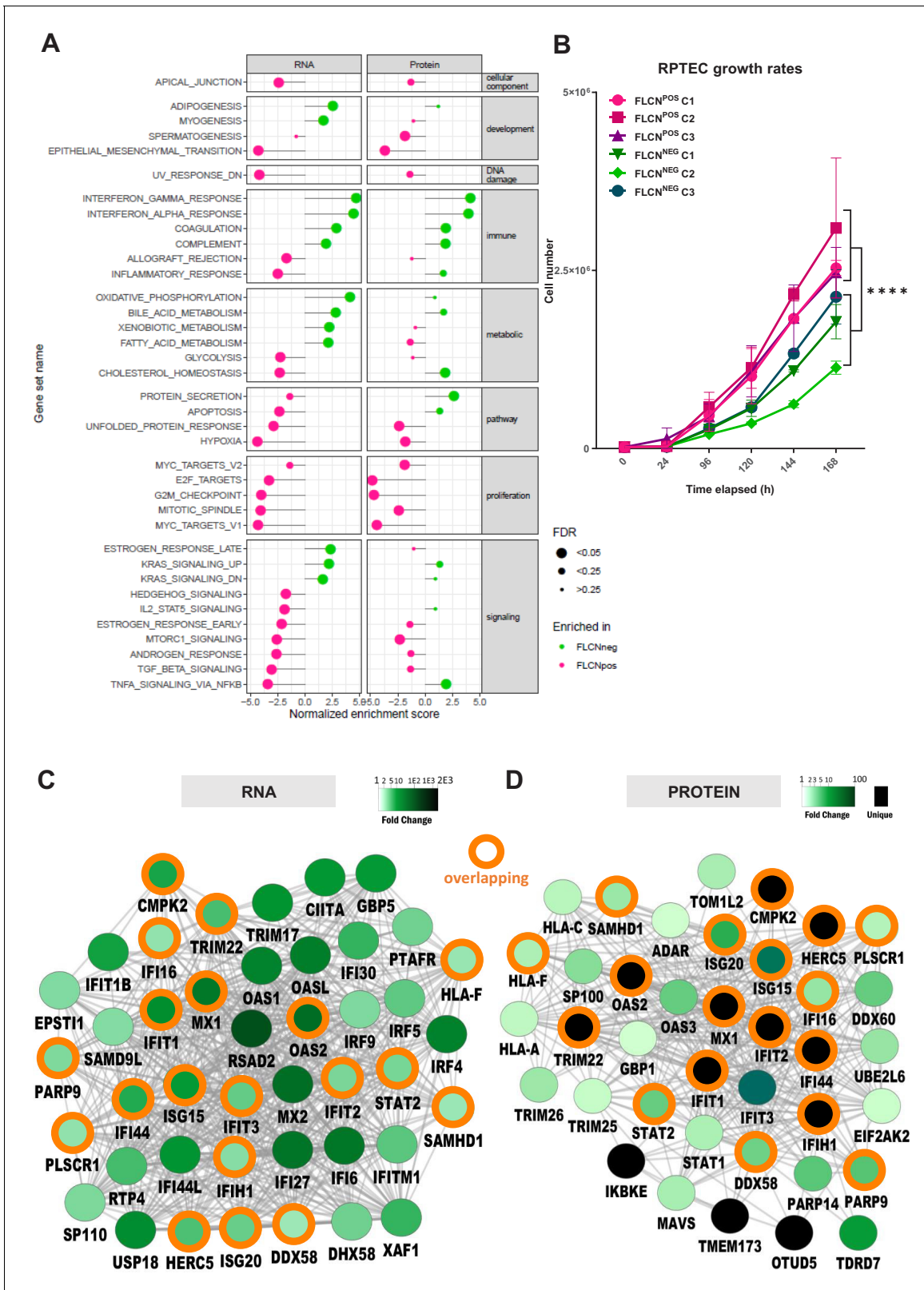


Figure 5. Gene set enrichment analysis reveals FLCN-dependent biological processes. (A) For Gene Set Enrichment Analysis (GSEA) genes or proteins were ranked based on p-values, with genes/proteins that are expressed significantly higher in FLCN^{NEG} RPTECs shown on top of the list (hallmark gene sets, classic ES). Enriched hallmark gene sets are ranked by normalized enrichment score (NES). Gene sets enriched in FLCN^{NEG} are shown in green and gene sets enriched in FLCN^{POS} in pink. The size of the dot reflects the significance of the enrichment (FDR=false discovery rate). Only biological

Figure 5 continued on next page

Figure 5 continued

processes that were significant in either RNA and/or protein data are depicted in this Figure. An extended version with all identified gene sets is shown in **Figure 6—figure supplement 1A**. (B) FLCN^{NEG} RPTECs grow significantly slower ($p=8.31E-11$) when compared to FLCN^{POS} RPTEC. Cell lines were seeded in equal densities and total cell number was counted for 7 consecutive days. Results shown are representative for two independent experiments. (C) Gene Ontology (biological processes, BinGO) analysis of mRNAs higher expressed in FLCN^{NEG} RPTECs reveals highly overlapping (orange circles) clusters of immune- and interferon-response-related genes between both data sets. Shade of green nodes represents fold change. (D) Gene Ontology (biological processes, BinGO) analysis of proteins higher expressed in FLCN^{NEG} RPTECs reveals highly overlapping (orange circles) clusters of immune and interferon response related genes between both data sets. Shades of green nodes represent different levels of fold change. Black nodes indicate uniquely detected proteins in FLCN^{NEG} RPTEC.

analyses did not identify regulatory elements shared in both RNA and protein data (**Figure 6—figure supplement 1B**). Upregulation of E-box or ISRE motif-dependent genes induced by FLCN loss in our RNAseq and proteomics analyses are shown in **Figure 6E–H**. Significant induction of the ISRE targets MX1, ISG15, IRF9, IFIT1, STAT1, and STAT2 next to TFE3 and E-box targets GPNMB, RRAGD, FNIP2, CTSD, and SQSTM1 were validated by qPCR in **Figure 6—figure supplement 1C**. We then analyzed protein expression levels compared to normal human kidney lysates using mass spectrometry of two independent BHD kidney tumors (**Figure 6—figure supplement 1D and E**). Although full interpretation of these results awaits the analysis of a larger tumor sample size, we observed elevated expression of both the ISRE as E-box associated genes in FLCN^{NEG} BHD tumors (**Figure 6I**). Based on these results, we conclude that FLCN loss upregulates two major gene classes: TFE3/TFEB regulated E-box targets and IFN-associated ISRE targets. Our integrated analysis reveals these genes and their protein products as candidate positive biomarkers for FLCN loss in BHD-related kidney cancer.

FLCN-FNIP1/2 loss upregulates STAT2 in a cell-type-specific manner

FLCN acts in a protein complex with FNIP1 and FNIP2 (Baba et al., 2006; Hasumi et al., 2015; Hasumi et al., 2008). When FNIP1 and FNIP2 are inactivated simultaneously, mice develop kidney cancer (Hasumi et al., 2015). To investigate whether deletion of both FNIP1 and FNIP2 in RPTEC had a molecular effect similar to that of FLCN loss, we created a FNIP1/FNIP2^{NEG} RPTEC cell line (**Figure 7—figure supplement 1A**) and analyzed gene induction. This confirmed that upregulation of ISRE or E-box motif genes is specifically connected to inactivation of the FLCN-FNIP1/FNIP2 axis (**Figure 7A**). Furthermore, TFE3 localized to the nucleus upon FNIP1/2 loss (**Figure 7—figure supplement 1B**).

Having validated a new gene program targeted by the FLCN-FNIP1/2 complex in RPTECs, we next determined whether FLCN-dependent control of ISRE target genes occurred in cells of different tissue origin, too. Using a similar approach as in RPTEC, we created a FLCN^{NEG} retinal pigment epithelial cell line (RPE1/TERT tet-on Cas9 TP53^{KO} Benedict et al., 2020; **Figure 7—figure supplement 1C**). Quantitative RT-PCR analyses revealed that, strikingly, ISRE and E-box associated genes were not induced in RPE1 cells by FLCN loss (**Figure 7B**). RRAGD was the only exception yet was induced ~10 times less strongly in RPE1 as compared to RPTEC cells. These results indicate that the two main gene induction programs directed by FLCN-FNIP1/2 are renal specific.

To identify the dominant signature of regulatory elements responding to FLCN loss in RPTEC, we further looked into the shared hits of RNA and protein data sets. Upon selecting the most significantly overlapping effects (FDR < 0.01, n = 181) (**Figure 7C**), iRegulon analysis of differential RNAs overlapping with differential proteins (r > 0.8, n = 49) upon FLCN loss predicted STAT1 and STAT2-binding motifs as the most enriched upstream regulatory elements (**Figure 7D**).

To prove that these upregulated gene programs were truly FLCN dependent, we complemented FLCN^{NEG} RPTEC C2 by re-introducing FLCN (**Figure 7—figure supplement 1D**). FLCN re-expression in FLCN^{NEG} RPTEC C2 restored regulation of TFE3 localization and nutrient sensing (**Figure 7—figure supplement 1E**). Moreover, re-introducing FLCN completely reverted the ISRE expression phenotype (**Figure 7E**). To confirm the roles of STAT1/2, we knocked them down using siRNAs in FLCN^{NEG} RPTEC C2. Quantitative RT-PCR showed that upregulation of the ISRE-associated gene program was entirely STAT1/2-dependent (**Figure 7E**). In addition, immunoblotting subcellular fractions showed higher protein levels of both STAT1 and STAT2 in FLCN^{NEG} cells (**Figure 7F**).

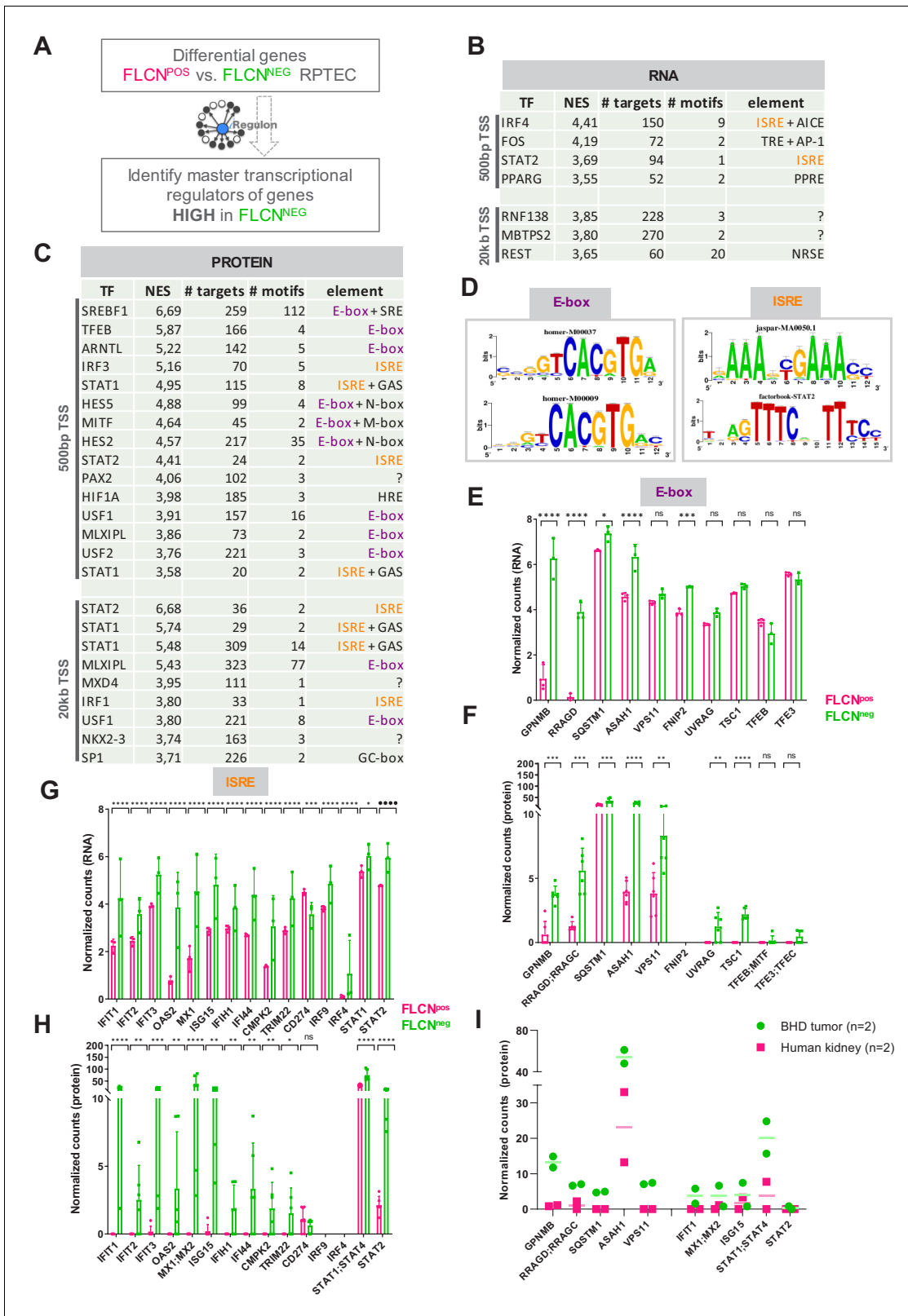


Figure 6. Identification of regulatory elements activated by FLCN loss in RPTEC and BHD tumors. (A) Identification of transcriptional regulatory elements associated with loss of FLCN expression. Regulons were identified by iRegulon (Janky et al., 2014), using an input a list of differential expressed genes (Figure 3). (B) Upstream regulons enriched in $FLCN^{NEG}$ RPTEC based on significantly upregulated genes derived from our transcriptomic data set ($n = 711$, $FDR < 0.05$ and $\logFC > 2$). Transcription factors with normalized enrichment scores (NES) higher than 3.5 are shown, Figure 6 continued on next page

Figure 6 continued

together with detected number of targets, motifs, and elements. ISREs are highlighted in orange. Upper part shows motifs enriched 500 bp upstream from transcription start site (TSS), lower part shows motifs enriched 20 kb around TSS. (C) Upstream regulons enriched in FLCN^{NEG} RPTEC based on significantly upregulated proteins derived from our proteomic data set (n = 498, p < 0.05 and FC > 2). Transcription factors with normalized enrichment score (NES) higher than 3.5 are shown, together with number of targets, motifs, and elements detected. ISREs are highlighted in orange and E-boxes in purple. STAT1 appears twice due to the fact that iRegulon ranks this transcription factor to be the most likely upstream regulator for two sets of targets genes, containing slightly different ISRE-motifs 20 kb upstream from the TSS. (D) Two major enriched motif elements detected in iRegulon analysis of genes upregulated in FLCN^{NEG} RPTEC. Regulons can be assigned to E-box (in purple) or ISRE (in orange) motif group. (E) Bar graphs of RNA expression levels of genes associated with an E-box motif, derived from RPTEC transcriptomic data set. FLCN^{POS} values are shown in pink and FLCN^{NEG} values are shown in green. Significant p-values are indicated as * ≤ 0.05, ** ≤ 0.01, *** ≤ 0.001, **** ≤ 0.0001. (F) Bar graphs of protein expression levels of genes associated with an E-box motif, derived from RPTEC proteomic data set. FLCN^{POS} values are shown in pink and FLCN^{NEG} values are shown in green. FNIP2 peptides were not detected in our proteomic experiment and therefore absent in the bar graph. Significant p-values are indicated as * ≤ 0.05, ** ≤ 0.01, *** ≤ 0.001, **** ≤ 0.0001. (G) Bar graphs of RNA expression levels of genes associated with an ISRE motif derived from RPTEC transcriptomic data set. FLCN^{POS} values are shown in pink and FLCN^{NEG} values are shown in green. Significant p-values are indicated as * ≤ 0.05, ** ≤ 0.01, *** ≤ 0.001, **** ≤ 0.0001. (H) Bar graphs of protein expression levels of genes associated with an ISRE motif derived from RPTEC proteomic data set. FLCN^{POS} values are shown in pink and FLCN^{NEG} values are shown in green. IRF9 and IRF4 peptides were not detected in our proteomic experiment and therefore absent in the bar graph. Significant p-values are indicated as * ≤ 0.05, ** ≤ 0.01, *** ≤ 0.001, **** ≤ 0.0001. (I) Dot plot of protein expression levels of genes associated with an E-box (left) or ISRE motif (right) derived from BHD kidney tumor proteomic data sets (see **Figure 6—figure supplement 1D and E**), as compared to normal kidney tissue. FLCN^{POS} values are shown in pink and FLCN^{NEG} values are shown in green. STAT2 levels were below detection levels in these protein extracts.

The online version of this article includes the following source data and figure supplement(s) for figure 6:

Figure supplement 1. Extended GSEA and iRegulon analysis of FLCN loss in RPTEC and BHD tumors.

Figure supplement 1—source data 1. Raw qRT-PCR values and fold change calculations belonging to **Figure 6—figure supplement 1C**.

Importantly, nuclear STAT2 was exclusively bound to chromatin in the absence of FLCN (**Figure 7G**) identifying STAT2 as a key target of FLCN.

Canonical IFN signaling follows IFN α or IFN γ stimulation of IFN receptors, resulting in auto-phosphorylation of Janus Kinases 1/2 (JAK1/JAK2) and Tyrosine Kinase 2 (TYK2). As a consequence, STAT1 and STAT2 are phosphorylated enabling formation of (homo)dimers or the ISGF3 complex (composed of STAT1, STAT2, and IRF9) which translocate to the nucleus to initiate transcription of ISRE genes (*Majoros et al., 2017*). To understand how STAT2 is activated upon FLCN loss, we measured IFN levels in supernatant of FLCN^{NEG} RPTEC cell lines, using a flow-cytometry-based cytometric bead array (CBA) or an enzyme-linked immunosorbent assay (ELISA). However, we did not detect any secreted IFN γ or IFN α , indicating that autocrine stimulation of IFN signaling did not cause the upregulated ISRE gene program or chromatin binding of STAT2 in FLCN^{NEG} RPTEC (**Figure 7—figure supplement 1F**). Also, we did not detect IFNA, IFNB and IFNG expression, nor differential expression of the IFN receptors (IFNAR1, IFNAR2, IFNGR1 and IFNGR2) in FLCN^{NEG} RPTEC (**Figure 7—figure supplement 1G**). Finally, in a recent phospho-proteomic analysis of our FLCN^{NEG} cell lines (not described in this paper), loss of FLCN did not lead to phosphorylation of upstream kinases JAK2 and TYK, or STAT2 itself. Lack of induced STAT1 phosphorylation as detected by immunoblot further confirmed that FLCN^{NEG} cells do not activate the IFN receptor (**Figure 7—figure supplement 1H**). Together, these results show that FLCN loss in RPTEC leads to a non-canonical, IFN-independent activation of unphosphorylated STAT1 and STAT2.

FLCN loss counteracts TFE3-induced hyperproliferation

As the experiments described above confirm our hypothesis that both TFE3 and STAT2 are FLCN targets, we started to investigate their potential contribution to renal cell transformation in vitro. We aimed to compare the effect of TFE3 activation resulting from FLCN loss to that of an active TFE3 gene fusion that is constitutively nuclear. Xp11 translocation RCC is a rare subtype of kidney cancer associated with various TFE3, *TFEB*, or *MITF* gene fusions, resulting in oncogenic, nuclear forms of these transcription factors (*Caliò et al., 2019*). This type of RCC behaves remarkably aggressively, with poor progression-free survival rates (*Lee et al., 2018*). One common fusion partner for TFE3 is the DNA-binding splicing factor SFPQ (*PSF*), which we expressed in RPTEC. For comparison, we created a new, diploid FLCN knock-out cell line by a recently improved gRNA and Cas9 delivery protocol (**Figure 8—figure supplement 1A and B**). In both SFPQ-TFE3 and FLCN^{KO} RPTEC cell lines, we confirmed high expression of TFE targets GPNMB, Rragd, FNIP2, and WIPI1 (**Figure 8A**). TFE3 or

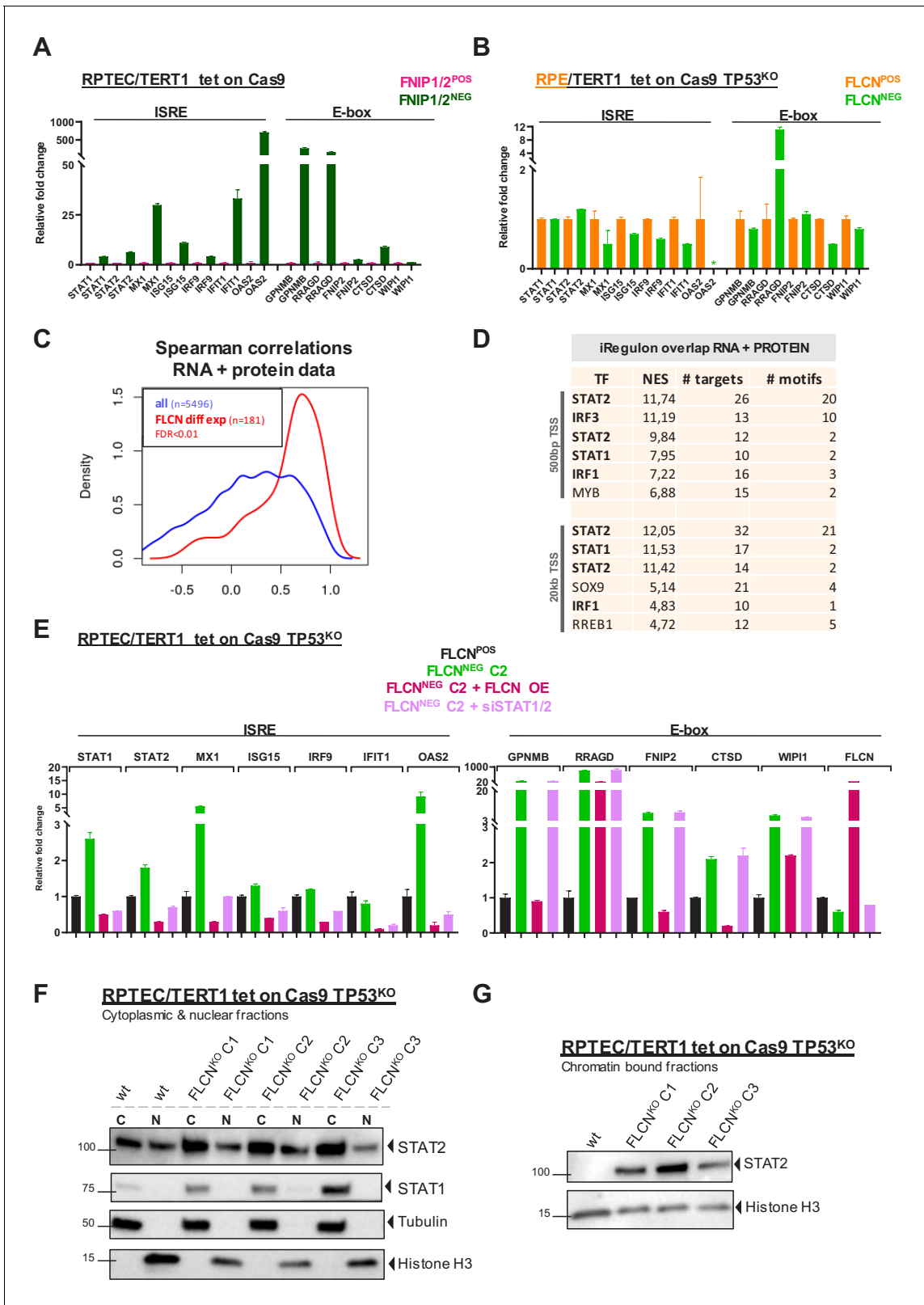


Figure 7. Inactivation of the FLCN-FNIP1/2 axis activates STAT2 in renal cells. (A) qRT-PCR levels of genes with ISRE or E-box motif in FNIP1^{POS}/FNIP2^{POS} and FNIP1^{NEG}/FNIP2^{NEG} RPTEC cells reveal that the identified FLCN-dependent gene signature is also induced upon loss of FLCN interacting proteins FNIP1 and FNIP2. Results shown are representative for two independent experiments with three technical replicates. To determine quantitative gene expression data levels were normalized to the geometric mean of two housekeeping genes. See **Figure 7—source data 1** for raw *Figure 7 continued on next page*

Figure 7 continued

qRT-PCR values and fold change calculations. (B) qRT-PCR levels of genes with ISRE or E-box motif in FLCN^{POS} and FLCN^{NEG} retinal pigment epithelial cells (RPE/TERT1 tet on Cas9 TP53^{KO}) reveal that the identified FLCN dependent gene signature is absent in an epithelial cell type of another tissue origin. Results shown are representative for two independent experiments. To determine quantitative gene expression data levels were normalized to the geometric mean of two housekeeping genes. *OAS2 level in FLCN^{NEG} RPE was too low to detect using qRT-PCR. See **Figure 7—source data 1** for raw qRT-PCR values and fold change calculations. (C) Spearman correlation analysis reveals overlapping FLCN-dependent RNA and protein data. FLCN differential mRNAs and proteins (FDR < 0.01, n = 181, red line) showed a higher correlation than the overlap of all identified mRNAs and proteins in our datasets (blue line). Statistical methods are described in Materials and methods section. (D) iRegulon analysis of differentially expressed genes (FDR < 0.01) with highest correlation with differentially expressed proteins (r > 0.8, n = 49) reveal STAT1, STAT2, IRF1, and IRF3 as most obvious upstream transcriptional regulators. Only regulons displaying normalized enrichment scores (NES) > 4.5 are shown. STAT2 appears twice due to the fact that iRegulon ranks this transcription factor to be the most likely upstream regulator for two sets of target genes, containing slightly different ISRE-motifs upstream from the transcription start site (TSS). (E) Reintroducing FLCN (overexpression, OE) or siRNA-mediated knock down of STAT1/STAT2 (10 nM, 72 hr) revert the IFN expression gene signature induced by FLCN loss in RPTEC FLCN^{NEG} C2. FLCN OE also lowers the enhanced expression of E-box-associated target genes but knock down of STAT1/2 has no effect on E-box-associated genes. Expression levels were determined by qRT-PCR and are representative of two independent experiments. To determine quantitative gene expression data levels were normalized to the geometric mean of two housekeeping genes. See **Figure 7—source data 1** for raw qRT-PCR values and fold change calculations. (F) Western blots of subcellular fractionated samples show higher expression of STAT1 and STAT2 in FLCN^{NEG} RPTEC as compared to FLCN^{POS} RPTEC. STAT2 was also detected in both cytoplasmic and nuclear fractions. Tubulin and histone H3 levels were used as loading control and to distinguish each fraction (N=nuclear, C=cytoplasmic). Results shown are representative of two independent fractionations. (G) Western blot of subcellular fractionated samples shows enhanced STAT2 DNA binding in FLCN^{NEG} RPTEC. Results shown are representative of three independent fractionations.

The online version of this article includes the following source data and figure supplement(s) for figure 7:

Source data 1. Raw qRT-PCR values and fold change calculations belonging to 7A, 7B and 7E.

Figure supplement 1. Validation of FLCNs role in the IFN response in additional cell models.

the constitutively active SFPQ-TFE3 fusion protein are both bound to chromatin fractions of FLCN^{KO} RPTEC or SFPQ-TFE3 RPTECs, respectively (**Figure 8B**). Knock down of TFE3/TFEB in the new TP53 wild-type FLCN^{KO} RPTEC cell line confirmed that TFE is required for the E-box expression program induced by FLCN loss (**Figure 3D**, **Figure 8—figure supplement 1C**).

Importantly, SFPQ-TFE3 expression did not induce IFN response genes in RPTECs, showing that the IFN gene induction signature is a specific effect of FLCN loss (**Figure 8A**). Concordantly, STAT2 recruitment to chromatin was enhanced in the absence of FLCN but not detected after expression of SFPQ-TFE3 (**Figure 8B**).

In agreement with the known growth inhibitory effects of the IFN stimulated gene program, but unexpected considering that FLCN is a tumor suppressor gene, FLCN loss reduced RPTEC colony formation and slowed cellular proliferation, regardless of TP53 status (**Figure 8C** upper panels, **Figure 5B**). Indeed, re-introducing FLCN expression in FLCN^{KO} RPTEC rescued cellular proliferation (**Figure 8D**). Reversely, the absence of FLCN dominantly repressed the hyper-proliferative effects of an active, oncogenic TFE3 fusion protein in RPTEC, similar to the growth reduction observed after treating SFPQ-TFE3 RPTECs with 100 IU/ml IFN γ (**Figure 8C** lower panels, **Figure 8E**). The growth inhibitory effect of knocking out FLCN in SFPQ-TFE3 RPTECs also correlated with strong induction of ISRE genes (**Figure 8—figure supplement 1D**). In conclusion, these results show that FLCN loss induces a STAT2-mediated IFN signature that results in growth inhibition, which counteracts the hyperproliferative effects of constitutive activation of TFE3 (**Figure 8—figure supplement 1E**). This indicates that, next to its growth stimulatory effects on cell proliferation via TFE3 activation, loss of FLCN also has a growth suppressive effect executed by STAT2 activation in renal tubular cells. STAT2 activation may also contribute to a pro-oncogenic state by contributing to an inflammatory response (**Figure 8—figure supplement 1E**). Determining the role of STAT2 activity in tumorigenesis will require further analysis of bio-markers and immune-infiltrates in a large set of BHD tumors.

Discussion

FLCN, together with its binding partners FNIP1 and FNIP2, forms a regulatory protein complex found in species ranging from yeast to humans (Nookala et al., 2012; Pacitto et al., 2015; Zhang et al., 2012). Pleiotropic effects resulting from its mutation in different model systems have hampered a clear understanding of the biological function of the FLCN-FNIP1/2 axis. At the organismal level, FLCN also plays different roles in different tissues. This is already apparent from the clinical

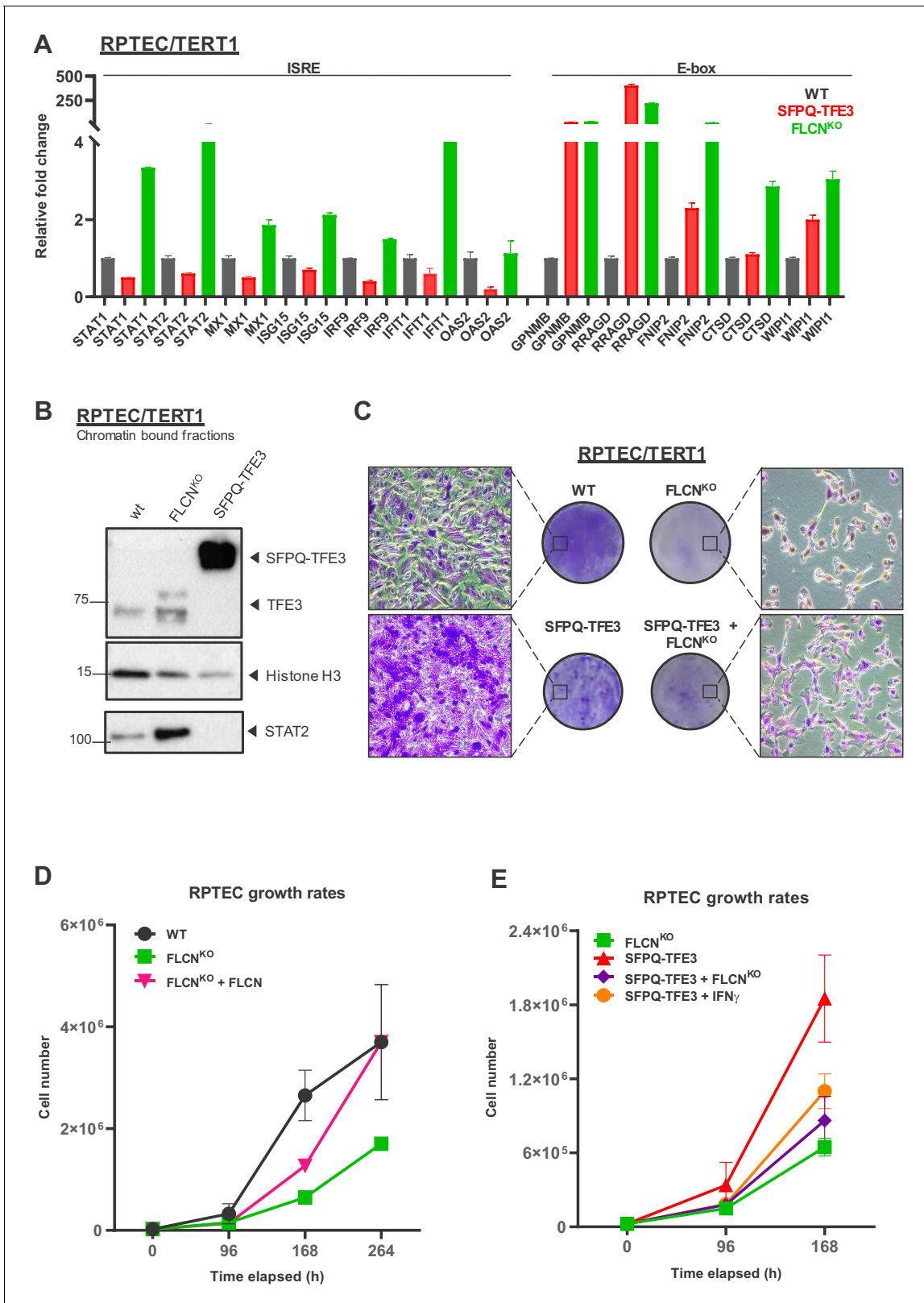


Figure 8. FLCN loss induces an interferon signature which counteracts growth promoting effects of active TFE3 in renal tubular cells. (A) Expression of a constitutively active SFPQ-TFE3 fusion protein in RPTEC results in upregulation of E-box-associated targets but does not induce enhanced expression of ISRE-associated genes. FLCN^{KO} RPTEC cells show both upregulation of E-box and ISRE-associated genes. Expression levels were determined by qPCR and are representative of two independent experiments. To determine quantitative gene expression data, levels were normalized to the *Figure 8 continued on next page*

Figure 8 continued

geometric mean of two housekeeping genes. See **Figure 8—source data 1** for raw qRT-PCR values and fold change calculations. (B) Western blots of subcellular fractions show enhanced binding of TFE3 to DNA in FLCN^{NEG} RPTEC and SFPO-TFE3 RPTEC. STAT2 DNA-binding was enhanced upon FLCN loss but reduced by SFPO-TFE3 over-expression in RPTEC. STAT2 was blotted on separate blots of the same lysates. Histone H3 levels were used as loading control and as marker for chromatin fraction. Western blot was performed two times, using independent fractionations. (C) Colony formation assays show that loss of FLCN in wild-type or SFPO-TFE3 RPTEC reduces colony outgrowth. SFPO-TFE3 RPTEC show more colonies than wild type RPTEC after 10 days. Insets show bright field images ($\times 20$ magnification). Cells were seeded in three technical replicates and experiment was performed twice. (D) Loss of FLCN in RPTEC results in slower growth, which is reverted when FLCN expression is restored by over-expression. Cell lines were seeded in equal densities and total cell numbers were counted three times within 11 days. Results shown are representative for two independent experiments. (E) Treatment with IFN γ (100IU/ml) or combining FLCN^{KO} in SFPO-TFE3 RPTEC results in growth inhibition. Cell lines were seeded in equal densities and total cell number was counted twice within 7 days. Results shown are representative for two independent experiments. The growth curve of FLCN^{KO} RPTEC (D) is added for comparison.

The online version of this article includes the following source data and figure supplement(s) for figure 8:

Source data 1. Raw qRT-PCR values and fold change calculations belonging to **Figure 8A** and **Figure 8—figure supplement 1C and D**.

Figure supplement 1. Creation and validation of FLCN^{NEG} and SFPO-TFE3 RPTECs.

manifestations in BHD syndrome, varying from fibrofolliculomas of the skin, to pulmonary cysts with increased risk for pneumothorax, and renal cysts associated with increased cancer risk (*Birt et al., 1977; Houweling et al., 2011; Nickerson et al., 2002; Schmidt et al., 2005; Zbar et al., 2002*).

While manifestations in the skin and lung in BHD probably reflect an effect of FLCN haplo-insufficiency, kidney tumorigenesis in BHD carriers starts by complete functional inactivation of the remaining wild type FLCN allele (*van Steensel et al., 2007; Vocke et al., 2005*). Here, we modeled the molecular and cellular effects of FLCN inactivation in the cell type most relevant for kidney tumorigenesis. The RPTEC/TERT1 cell line is widely accepted as an appropriate in vitro model system for human kidney function (*Aschauer et al., 2015*). Nevertheless, it is important to emphasize that many of our conclusions are based on independent clones derived from a single human cell line. Here, we observed that loss of FLCN had three main effects in RPTEC/TERT1: (1) severely reduced cellular proliferation, regardless of TP53 activity or alterations in karyotype; (2) nuclear accumulation and activation of TFE3, concomitant with TFE3/TFEB-dependent upregulation of a specific set of E-box genes linked to autophagy and lysosomal control; (3) IFN-independent upregulation and chromatin binding of STAT2, activating a gene program of typical IFN response genes, possibly in cooperation with STAT1. Upregulated genes besides STAT1 and STAT2 include MX1, IFIT1, ISG15, IRF9, and OAS2. We found the combination of these two master gene programs to be a renal-specific response to FLCN inactivation, also observed after knocking out FNIP1 and FNIP2. Re-expressing FLCN reverted these effects, proving that they are specific to FLCN loss.

How these gene expression programs contribute to oncogenesis needs to be resolved, but TFE3 activation was clearly sufficient to promote uncontrolled, enhanced proliferation and loss of contact inhibition in RPTEC cells (e.g. **Figure 8**). Knocking out *FLCN* in the context of active TFE3 slowed cellular proliferation to the level observed after IFN γ treatment. The upregulated IFN signature could thus explain why loss of the FLCN tumor suppressor, paradoxically, represses cellular proliferation. In relation to cancer, slow growth induced by FLCN loss and STAT2 upregulation may form a barrier to TFE3-driven renal tumorigenesis in BHD patients. On the other hand, it is possible that the activation of the IFN program is associated with a pro-oncogenic inflammatory response. The TFE3 and IFN signature programs are connected in this respect: TFE3/TFEB upregulate cytokines in macrophages that elicit an innate immune response linked to pathogen resistance (*El-Houjeiri et al., 2019*). In our RPTEC FLCN^{NEG} cell models however, we observed a clear downregulation in secreted cytokine IL-8 and no consistent changes in IL-6 expression (data not shown), suggesting that, at least in renal cells, the IFN program induced by FLCN inactivation is not connected to inflammation *per se*.

Preliminary analysis of BHD tumor material showed the presence of immune cells at tumor margins (unpublished findings) and upregulation of ISRE genes (**Figure 6I**). Collectively our data lead to the hypothesis that renal tumorigenesis in BHD patients could follow two different paths: either pro-inflammatory effects of specific E-box and/or ISRE genes are further aggravated by secondary mutations during tumor evolution, or growth-suppression by IFN signature genes, which is dominant over the effects of TFE3 activation, is gradually lost by additionally acquired mutations thus leading to

TFE3-driven tumor progression. This suggests that certain IFN response genes which strongly reduce proliferation form a deeper tumor suppressive layer protecting against uncontrolled proliferation in the absence of sufficient FLCN expression. This hypothesis fits with the observation that renal tumors specifically driven by TFE3 activation behave more aggressively as compared to slowly growing BHD tumors. Speculatively, BHD tumors fall into two mutually exclusive classes, with either high or low IFN signatures and/or STAT2 expression depending on their growth properties.

From our results, it is clear that FLCN loss promotes STAT2 binding to chromatin but we did not resolve a clear mechanism by which FLCN loss promotes these changes. Because TFE3 activation is not sufficient to induce STAT2 or upregulate ISRE genes, and reciprocally STAT1/2 siRNA does not downregulate the E-box genes, we conclude that the two gene activation programs are separate effects of FLCN loss. We considered that FLCN might affect STAT2 protein stability, in a similar manner as observed for a number of viral proteins that bind directly to STAT2 (*Grant et al., 2016; Morrison et al., 2019*) but found no evidence for direct complex formation between STAT2 and FLCN. Also, the protein half-life of STAT2 was similar in the absence of FLCN and no shift was observed in STAT2 nucleo-cytoplasmic distribution (data not shown).

With respect to candidate TFE3 target genes that drive renal epithelial cell transformation, it is clear that in the absence of FLCN, particularly GPNMB, RRAGD, ASAH1 and FNIP2, the latter in an apparent feedback mechanism, are strongly upregulated. In renal cells lacking FNIP1 and FNIP2, GPNMB and RRAGD are also very strongly induced. This illustrates the potential value of GPNMB and RRAGD as positive biomarkers for FLCN inactivation such as in BHD tumors.

GPNMB is a transmembrane protein frequently upregulated in a wide variety of tumors, including lung and renal cancer, yet it is unclear whether GPNMB overexpression in itself is tumorigenic (*Taya and Hammes, 2018*). Importantly, GPNMB can be targeted therapeutically using antibody-drug conjugates which are in clinical trials for cancer therapy, such as *glembatumumab vedotin* (*Rose et al., 2017*), providing an entry point for the evaluation of *glembatumumab* in the treatment of BHD tumors. Furthermore, RRAGD is a candidate oncogenic target gene of TFE3, previously associated with loss of FLCN (*Di Malta et al., 2017; Tsun et al., 2013*). Recently, *Napolitano et al., 2020* described TFEB to be the main driver of kidney abnormalities in a BHD mouse model. Their results show that TFEB is phosphorylated by mTORC1 in substrate-specific mechanism that is mediated by Rag GTPases. FLCN is a key regulator of Rag GTPases but despite the fact that we found clear upregulation of both RagC and RagD, we found no evidence for mTORC1 hyperactivation in our human in vitro model system. There might be crucial differences in renal tumorigenesis between mice and humans, where mTORC1 activation may occur at a later stage in oncogenic transformation of FLCN^{NEG} renal epithelial cells.

In addition to the upregulated TFE3 and ISRE programs, we observed that several genes were downregulated by FLCN loss. GSEA analyses of downregulated genes showed overlapping biological processes but iRegulon analyses failed to reveal a clear common upstream transcriptional regulator of these genes in mRNA and protein data. Taken together however, the repository of FLCN target genes and proteins presented here provides a clear basis for further investigations into specific roles in kidney cancer and other BHD-related symptoms. This could facilitate the discovery of biomarkers for early-stage tumorigenesis and therapeutic strategies to prevent or treat RCC metastases in BHD patients.

Materials and methods

Cell culture

Renal proximal tubular epithelial cells (RPTEC/TERT1, ATCC CRL-4031) were maintained in DMEM/F12 (Gibco, Life Technologies, Thermo Fisher Scientific Inc, Waltham, Massachusetts, US) according to the manufacturer's protocol with addition of 2% fetal bovine serum (FBS, Gibco). To maintain the selective pressure for immortalization 0.1 mg/ml G418 Sulfate (Calbiochem, Merck, Darmstadt, Germany) was added. Cell lines were cultured in a humidified atmosphere at 37°C and 5% CO₂. Retinal pigment epithelial cells (RPE-1/hTERT, ATCC CRL-4000) were maintained in DMEM (Gibco, Life Technologies) with addition of 8% FBS and 1 mM Sodium Pyruvate (Gibco, Life Technologies). The generation of used RPE1-hTERT tet-on Cas9 TP53^{KO} cells was described earlier (*Benedict et al., 2020*). Both cell lines were obtained recently from ATCC and experiments were performed

exclusively with low-passage cell lines which were regularly tested to exclude Mycoplasma infections; follow-up authentication was performed on the basis of functional assays, gene expression patterns and cellular morphology.

Karyotype analysis

After standard cytogenetic harvesting and GTG banding, at least 35 metaphase cells were analyzed and described according to ISCN 2016 (McGowan-Jordan *et al.*, 2016).

Virus production and infection

To create an inducible Cas9 RPTEC cell line, lentiviral production and transduction took place according to the Lenti-X Tet-On 3G Inducible Expression System (Clontech, Takara Bio, Japan) technical manual. In short, Cas9 cDNA was cloned into the pLVX-Tre3G plasmid where after Tre3G-Cas9 and Tet3G lentiviral particles were produced in HEK293T cells. For transduction RPTEC cells were seeded (250 k/well) in a 6-wells plate one day prior to infection. The next day growth media was removed and 1 ml media containing viruses was added. Cells were incubated overnight and after 24 hr media was replaced with 2 ml fresh media. The next day cells were transferred to 10 cm plates and Puromycin (3 µg/ml, Sigma-Aldrich, St. Louis, Missouri, USA) was added to select for successfully transduced cells. G418 was already present in growth media to maintain selective pressure for immortalization and therefore not added for Tet3G selection. For FLCN rescue experiments FLCN cDNA was cloned into pLenti CMVie-IRES-BlastR (gift from Ghassan Mouneimne, Addgene plasmid #119863 [Puleo *et al.*, 2019]). The SFPO-TFE3 fusion sequence was derived from gene expression analysis of a patient-derived pediatric RCC (Calandrini *et al.*, 2020) and subsequently cloned as geneblock into pLKO-Ubc lentiviral backbone (Fumagalli *et al.*, 2017) using Gibson assembly. For both lentiviral particles were produced in HEK293T and transduced into RPTEC. Blasticidin (15 µg/ml, Invitrogen, Life Technologies) was added for selection of successfully transduced cells and protein overexpression was confirmed by western blotting.

CRISPR/Cas9 gene editing

For gRNA transfections, RPTEC tet-on Cas9 cells were seeded (75 k cells/well) in 24-well plates with Doxycycline [10 ng/ml, Sigma-Aldrich] at day 0 to induce Cas9 expression. The next day transfection reagent RNAiMAX (Lipofectamine RNAiMAX Transfection Reagent, Thermo Fischer Scientific) was diluted in serum-free medium (Optimem, Gibco, Life Technologies), mixed with gRNA complex (10 uM crRNA and 10 uM tracrRNA, Dharmacon, Horizon Discovery, Cambridge, United Kingdom) and dropwise added to the cells. gRNAs were designed using crispr.mit.edu design tool. Following crRNA sequences were used: FLCN_exon 5 (GTGGCTGACGTATTTAATGG) FLCN_exon 7 (TGTCAGCGATGTCAGCGAGC), TP53_exon 4 (CCATTGTTCAATATCGTCCG), FNIP1_exon 2 (GATA TACAATCAGTCGAATC), and FNIP2_exon 3 (GATGGTTGTACCTGGTACTT).

After 24 h cells were transferred to 10 cm plates and Nutlin-3 (10 µM, Selleck Chemicals, Houston, Texas, USA) was added for selection of TP53 knock-out and thus successfully transfected cells. After selection cells were grown in limiting dilution in 96-wells plates to generate single cell clones. Subsequently, knockout status was assessed by western blot and Sanger sequencing. FLCN^{KO} RPTEC cell line described in **Figure 8** was created using Synthego's Synthetic cr:tracrRNA Kit and corresponding manual. Cas9/gRNA (FLCN_exon 4 GAGAGCCACGAUGGCAUUCA + modified EZ scaffold) RNP complexes were transfected transiently using Neon Electroporation System (Thermo-Fisher). Subsequently cells were grown in limiting dilution in 96-well plates to generate single-cell clones and knockout status was assessed by western blot and Sanger sequencing. Sequenced samples were analyzed by manual alignment or using the Synthego ICE analysis (ice.synthego.com) tool which gives a quantitative spectrum of *indels* that are formed around the cut site.

siRNA-mediated knock down

For knock down synthetic siRNAs (siSTAT1_SMARTpool: L-003543-00-0005, siSTAT2_SMARTpool: L-012064-00-0005, siTFEB_SMARTpool: L-009798-00-0005, siTFE3_SMARTpool: L-009363-00-0005, siNT_pool 4: D-001210-04-05, Dharmacon) were transfected using RNAiMAX (Lipofectamine RNAiMAX Transfection Reagent, Thermo Fischer Scientific). After 72 hr 10 nM treatment cells were harvested and stored as dry cell pellet (~1.5E6 cells) in -20°C.

DNA isolation, PCR, and sequencing

DNA was extracted from dry cell pellet (~1.5E6 cells) according to technical manual of DNA isolation kit (QIAamp DNA Blood Mini Kit, Qiagen, Venlo, Netherlands). Subsequently equal amounts of DNA were amplified by PCR. Tubes were placed in a thermal cycler (Veriti, Thermo-Fischer Scientific) for amplification with specific PCR primer mixes (10 μ M). PCR program used for amplification was 1 cycle of 94°C for 3 min, 5 cycles of 94°C for 30 s, 65°C for 30 s, 72°C for 120 s, 30 cycles of 94°C for 30 s, 60°C for 30 s, 72°C for 2 min, 72°C for 10 min and ending in a rapid thermal ramp to 10°C. Here after PCR purification (ExoSAP-IT PCR product cleanup (USB products, Affymetrix, Santa Clara, California, USA) and Sephadex G-50 superfine gel (GE Healthcare, Chicago, Illinois, USA)) took place and samples were further analyzed by sequencing. Sequencing was either performed in-house or at Eurofins Genomics. For PCR and sequencing, following primers were used:

FLCN_4

Fw 5' GTAAAACGACGGCCAGGGAGGTTTCATGGAGTCAATAGG 3'

Rev 5' CAGGAAACAGCTATGACTGCTCTCAGGTCCTCC 3'

FLCN_5

Fw 5' GTAAAACGACGGCCAGACCTAAGAGAGTTTGTGCGCCCTG 3'

Rev 5' CAGGAAACAGCTATGAAGTGCCTGCCTCCCTGTGC 3'

FLCN_7

Fw 5' GTAAAACGACGGCCAGGGTCCGAGCTGCTGGCAG 3'

Rev 5' CAGGAAACAGCTATGACCAATGTATCGTACTGCTCTATC 3'

TP53

Fw 5' GAGACCTGTGGGAAGCGAAA 3'

Rev 5' GCTGCCCTGGTAGGTTTTCT 3'

FNIP1

Fw 5' GCCTTACCAGAGTTTGATCCA 3'

Rev 5' TCATTTCTTCTCCCTCAGC 3'

FNIP2

Fw 5' CAGTAGCAGCAGCAGCATCT 3'

Rev 5' TCTTCAGCATTCTGCCATCCCA 3'

M13

Fw 5' GTAAAACGACGGCCAG 3'

Rev 5' CAGGAAACAGCTATGA 3'

In-house sequencing was done according the BigDye Terminator v1.1 Sequencing Kit (Life Technologies) protocol. For each sample ~75 ng DNA and specific sequencing primers (3.3 μ M) were used. Tubes were placed in a thermal cycler for amplification with specific PCR primer mixes. PCR program used for amplification was: 1 cycle of 95°C for 1 min, 30 cycles of 95°C for 10 s, 55°C for 5 s, 60°C for 2 min and ending in a rapid thermal ramp to 10°C.

RNA extraction, sequencing and qRT-PCR

RNA was extracted from dry cell pellet (~1.5E6 cells) according to the High Pure RNA Isolation Kit (Roche, Penzberg, Germany) manual. For Illumina-based sequencing, samples were prepped using TruSeq Stranded mRNA Library Preparation Kit according to TruSeq Stranded mRNA Sample Preparation Guide. Sequencing was performed on an Illumina HiSeq 4000 (Illumina, San Diego, California, USA) using run mode SR50. Reads were trimmed using sickle-1.33 (Joshi and Fass, 2011) and aligned to hg19 using hisat2-2.0.4 (Kim et al., 2015). The alignments were assigned to genes and exons using featurecount-1.5.0-p3 (Liao et al., 2014) using the gene annotation provided by the iGenomes resource (Illumina, 2020). For quantitative RT-PCR we used Biorad iScript cDNA Synthesis Kit and LightCycler 480 FastStart DNA Master SYBR Green I (Roche). Measurements were performed with LightCycler 480 System and corresponding software (Roche). To determine the quantitative gene expression data levels were normalized to the geometric mean of two housekeeping genes. All experiments were at least performed in duplicate with three technical replicates per experiment. Primer sequences used in this study are:

GPNMB

Fw 5' CCTCGTGGGCTCAAATATAAC 3' Rev 5' TTTCTGCAGTTCTTCTCATAGAC 3'

RRAGD

Fw 5' CCTGGCTCTCGTTTGCTTTGTCAG 3' Rev 5' GGGGTGGCTCTTTTTCTTCTGC 3'

FNIP2
 Fw 5' GGCCTTGAAGTGGAGCTG 3' Rev 5' GTGAGCGGCCAAAGTTCCT 3'
 CTSD
 Fw 5' ccatTCCCGAGGTGCTCAAGAACTAC 3' Rev 5' GCAAGCGATGTCCAGCAGTTTG
 SQSTM1
 Fw 5' ATCGGAGGATCCGAGTGT 3' Rev 5' TGGCTGTGAGCTGCTCTT 3'
 WIPI1
 Fw 5' GTTGAAGACCCTCCTGGATATTCCTGC 3' Rev 5' gCAGACTGTTTTTCAGGGAGTTTCCA
 TC 3'
 STAT1
 Fw 5' CTACGAACATGACCCTATCAC 3' Rev 5' GCTGTCTTTCCACCACAA 3'
 ISG15
 Fw 5' GAGAGGCAGCGAACTCATCT 3' Rev 5' CTCAGCTCTGACACCGACA 3'
 IFIT1
 Fw 5' AGGATGAAGGACAGGAAG 3' Rev 5' GCAGTAAGACAGAAGTGG 3'
 MX1
 Fw 5' GACAATCAGCCTGGTGGTGGTC 3' Rev 5' GTAACCCTTCTTCAGGTGGAACACG 3'
 IRF9
 Fw 5' GGGAGCAGTCCATTCAGACA 3' Rev 5' CAGCAGTGAGTAGTCTGGCT 3'
 STAT2
 Fw 5' CCTCCTGCCTGTGGACATTCG 3' Rev 5' CAGCAACAAGGACTCTGGGTC 3'
 OAS2
 Fw 5' CAACCTGGATAATGAGTTACCTGC 3' Rev 5' CTGTTGATTGTGCGAAGCAGTTTTTC 3'
 HPRT1
 Fw 5' TGACACTGGGAAAACAATGCA 3' Rev 5' GGCCTTTTTACCAGCAAGCT 3'
 TBP
 Fw 5' TGCACAGGAGCCAAGAGTGAA 3' Rev 5' CACATCACAGCTCCCCACCA 3'
 FLCN
 Fw 5' GGAGAAGCTCGCTGATTTAGAAGAGGA 3' Rev 5' ACCCAGGACCTGCCTCATG 3'
 RRAGC
 Fw 5' GGTCTGCATTCTAAGGGAAGAA 3' Rev 5' GAAGTCACACCCACCTCAA 3'
 AMDHD2
 Fw 5' TGCTCTCAAGGCACCAAG 3' Rev 5' TGCCTCAGCACCAAAGT 3'
 GABARAP
 Fw 5' GGCGAGAAGATCCGAAAGAA 3' Rev 5' GATCAGAAGGCACCAGGTATT 3'
 ARHGAP12
 Fw 5' GATACCGGATTCACCAGGAATAG 3' Rev 5' GGGCGTCGTGTAAGAAACT 3'
 TFEB
 Fw 5' GCCTGGAGATGACCAACAA 3' Rev 5' CCAGCTCAGCCATGTCA 3'
 TFE3
 Fw 5' AACGACAGGATCAAGGAACTG 3' Rev 5' CGGCTCTCCAGGTCTTTG 3'

Both ISG15 and IFIT1 primers sequences were derived from previous studies (*Bektas et al., 2008; Labbé et al., 2012*).

Differential expression analysis of RNAseq data

We used the R package edgeR (*Robinson et al., 2010*) to compare RNA-sequencing profiles between FLCN^{POS} and FLCN^{NEG} replicates, as well as between TP53^{POS} and TP53^{NEG}. This involved reading in the gene-level counts, computing library-size normalizing factors using the trimmed-mean of M-values (TMM) method and then fitting a model to estimate the group effect. Obtained p-values were corrected for multiple testing using the Benjamini-Hochberg false discovery rate (FDR) step-up procedure (*Benjamini and Hochberg, 1995*).

Mass-spectrometry-based proteomics using GeLC-MS/MS

We applied our label-free GeLC-MS/MS-based proteomics workflow with alternating study design that has been extensively bench-marked for reproducibility (*Fratantoni et al., 2010; Piersma et al., 2010; Piersma et al., 2013*).

Sample preparation for LC-MS/MS

Equal protein lysates, of each cell line in duplicate, were separated on precast 4–12% gradient gels using NuPAGE SDS-PAGE (Invitrogen, Carlsbad, California, USA). Gels were fixed in 50% ethanol/3% phosphoric acid solution and stained with Coomassie R-250. Gel lanes were cut into five bands (see cutting scheme **Figure 2—figure supplement 2B**) and each band was cut into ~1 mm³ cubes. Gel cubes were washed with 50 mM ammonium bicarbonate/50% acetonitrile and were transferred to a microcentrifuge tube, vortexed in 50 mM ammonium bicarbonate for 10 min and pelleted. The supernatant was removed, and the gel cubes were again vortexed in 50 mM ammonium bicarbonate/50% acetonitrile for 10 min. After pelleting and removal of the supernatant, this wash step was repeated. Subsequently, gel cubes were reduced in 50 mM ammonium bicarbonate supplemented with 10 mM DTT at 56°C for 1 hr, where after supernatant was removed. Gel cubes were alkylated in 50 mM ammonium bicarbonate supplemented with 50 mM iodoacetamide for 45 min at RT in the dark. Next, gel cubes were washed with 50 mM ammonium bicarbonate/50% acetonitrile, dried in a vacuum centrifuge at 50°C and covered with trypsin solution (6.25 ng/μl in 50 mM ammonium bicarbonate). Following rehydration with trypsin solution and removal of excess trypsin, gel cubes were covered with 50 mM ammonium bicarbonate and incubated overnight at 25°C. Peptides were extracted from the gel cubes with 100 μl of 1% formic acid (once) and 100 μl of 5% formic acid/50% acetonitrile (twice). A total of 300 μl extracts were stored at –20°C until use. Prior to LC-MS, the extracts were concentrated in a vacuum centrifuge at 50°C, volumes were adjusted to 50 μl by adding 0.05% formic acid, filtered through a 0.45 μm spin filter, and transferred to a LC auto sampler vial.

LC-MS/MS

Peptides were separated by an Ultimate 3000 nanoLC-MS/MS system (Dionex LC-Packings, Amsterdam, Netherlands) equipped with a 45 cm × 75 μm ID fused silica column custom packed with 1.9 μm 120 Å ReproSil Pur C18 aqua (Dr Maisch GMBH, Ammerbuch-Entringen, Germany). After injection, peptides were trapped at 6 μl/min on a 10 mm × 100 μm ID trap column packed with 5 μm 120 Å ReproSil Pur C18 aqua in 0.05% formic acid. Peptides were separated at 300 nl/min in a 10–40% gradient (buffer A: 0.5% acetic acid (Fisher Scientific), buffer B: 80% ACN, 0.5% acetic acid) in 60 min (100-min inject-to-inject). Eluting peptides were ionized at a potential of +2 kV into a Q Exactive mass spectrometer (Thermo Fisher, Bremen, Germany). Intact masses were measured at resolution 70,000 (at m/z 200) in the orbitrap using an AGC target value of 3E6 charges. The top 10 peptide signals (charge-states 2+ and higher) were submitted to MS/MS in the HCD (higher-energy collision) cell (1.6 amu isolation width, 25% normalized collision energy). MS/MS spectra were acquired at resolution 17,500 (at m/z 200) in the orbitrap using an AGC target value of 1E6 charges, a maxIT of 60 ms, and an underfill ratio of 0.1%. Dynamic exclusion was applied with a repeat count of 1 and an exclusion time of 30 s.

Protein identification and label-free quantitation

MS/MS spectra were searched against the reference proteome FASTA file (42161 entries; swissprot_2017_03_human_canonical_and_isoform). Enzyme specificity was set to trypsin, and up to two missed cleavages were allowed. Cysteine carboxamidomethylation (Cys, +57.021464 Da) was treated as fixed modification and methionine oxidation (Met, +15.994915 Da) and N-terminal acetylation (N-terminal, +42.010565 Da) as variable modifications. Peptide precursor ions were searched with a maximum mass deviation of 4.5 ppm and fragment ions with a maximum mass deviation of 20 ppm. Peptide and protein identifications were filtered at an FDR of 1% using the decoy database strategy. The minimal peptide length was seven amino acids. Proteins that could not be differentiated based on MS/MS spectra alone were grouped into protein groups (default MaxQuant settings). Searches were performed with the label-free quantification option selected. Proteins were quantified by spectral counting, that is, the number of identified MS/MS spectra for a given protein (*Liu et al., 2004*) combining the five fractions per sample. Raw counts were normalized on the sum of spectral counts for all identified proteins in a particular sample, relative to the average sample sum determined with all samples. To find statistically significant differences in normalized counts between sample groups, we applied the beta-binomial test (*Pham et al., 2010*), which takes into account within-sample and between-sample variation using an alpha level of 0.05. For proteomic analyses of

tissue material, human kidney lysates (obtained commercially NB820-59231 (HK1) and sc-363764 (HK2)) and fresh BHD tumor tissues (BHDT1 and BHDT2, see details below) lysed in NP40 lysis buffer (50 mM Tris-HCl pH 7.4, 150 mM NaCl, 1% NP40) were used and analysed as described above.

Patient material

BHD T1 and BHD T2 tumor material was obtained with informed consent for research use according to Amsterdam UMC Medical Ethics Committee guidelines. Both tissues are leftover material from surgery isolated by a pathologist and stored at the Amsterdam UMC Birt-Hogg-Dubé biobank filed under number 2019.359.

Gene ontology and gene set enrichment analysis

Protein-protein relations were retrieved from the STRING database v11 (*Szklarczyk et al., 2019*) and imported as a network in Cytoscape v3.5.1 (*Shannon et al., 2003*). Enriched gene ontology terms (biological processes) were obtained with the BiNGO v3.0.3 app for Cytoscape (*Maere et al., 2005*), using hypergeometric testing with Benjamini-Hochberg multiple-test correction. Ontology analysis was performed with both the major connected component of the network and subclusters obtained with the ClusterONE v1.0 app for Cytoscape (*Nepusz et al., 2012*). Gene set enrichment was performed with GSEA software (*Subramanian et al., 2005*) using gene sets from Molecular Signatures Database v6.1 (*Liberzon et al., 2011*). Pre-ranked GSEA was performed with ranking by the statistics of the differential $FLCN^{NEG}$ - $FLCN^{POS}$ tests. As a ranking metric, we used the product of the sign of the fold change and the negative value of the log₁₀-transformed p-value. Visualization of results was performed in R using the ggplot2 package (*Wickham, 2016*).

Amino acid starvations and immunofluorescence

For immunofluorescence experiments RPTECs were grown on coverslips (15 mm diameter) on day 1. The medium was refreshed at the end of day 2 or replaced by serum free medium. Amino acid starvation was done with cells that had been serum starved overnight in custom-made DMEM without amino acids but containing 2 mM L-glutamine for 2 hr. Amino acid addback was done by adding an equal volume of starvation medium containing twice the amount of essential amino acids for 15 min. Next, cells were washed twice with ice-cold PBS and fixed in 4% para-formaldehyde for 20 min at room temperature. After washing with PBS, cells were permeabilized with 0.25% Saponin (Sigma Aldrich) in PBS and blocked with blocking solution (10% FCS, 0.25% Saponin in PBS). Coverslips were incubated overnight at room temperature with primary antibodies in blocking solution. The next day, coverslips were washed in 0.25% Saponin in PBS and incubated with secondary antibodies from Fisher Scientific (Alexa 488-goat anti-mouse; 10696113 and Alexa 568-goat anti-rabbit; A11036) for 2 hr at room temperature. Hereafter cells were mounted with Immu-Mount (Thermo Scientific Shandon). Specimens were visualized under Zeiss LSM510 microscope and imaged using Zeiss vision software. The following antibodies were used: mTOR (7C10, CST 2983; 1:300), Lamp2 (H4B4, Ab24631; Abcam; 1:400) and TFE3 (CST 14779; 1:300). For western blot analyses of starvation experiments, RPTECs were seeded in 6-wells plates and treated in like manner. Instead of fixation cells were scraped into 1x Laemmli sample buffer (Sigma Aldrich) and immunoblotted as described below. Starvations, as well as immunofluorescent stainings and immunoblotting were performed three times.

Immunoblotting

For immunoblotting dry cell pellets (~1.5E6 cells) were lysed in NP40 lysis buffer (50 mM Tris-HCl pH 7.4, 150 mM NaCl, 1% NP40) supplemented with protease and phosphatase inhibitors (Roche). Subsequently samples were boiled at 70°C for 5 min in 1x NuPAGE LDS sample buffer (Novex NP0007, Thermo-Fischer) with 10% 1M DTT (Sigma) and equal amounts were separated by 4–15% or 8–16% SDS-PAGE (BioRad) and blotted onto polyvinylidene fluoride (PVDF) transfer membranes (Merck). After transfer, membrane was blocked for 1 hr at room temperature with 5% milk (ELK, Campina, Amersfoort, Netherlands) in TBST. The primary antibody incubation was ON at 4°C in 2.5% milk in TBST. Next day, membrane was washed and incubated with appropriate secondary antibody (Dako) for 3 hr at 4°C in 2.5% milk in TBST. For detection of phosphorylated proteins, blocking and incubation steps were performed with Bovine Serum Albumin (BSA Fraction V, Roche) instead of milk. After

incubation the membrane was thoroughly washed where after bands were visualized by chemoluminescence (ECL prime, Amersham, VWR, Radnor, Pennsylvania, USA) in combination with ChemiDoc Imaging Systems (BioRad, Hercules, California, USA). For subcellular fractionation experiments the Subcellular Protein Fractionation Kit for Cultured Cells (78840, Thermo Scientific) was used according to manufacturer's protocol.

Antibodies

For western blot experiments following antibodies were used according to individual datasheets: Vinculin (H-10, sc-25336), FLCN (D14G9, CST 36975), Cas9 (epigentek A-9000-050), AQP1 (sc-25287), GPNMB (AF2550-SP), SQSTM1 (CST 88588), RRAGD (CST_4470S), FNIP1 (ab134969) FNIP2 (HPA042779), STAT2 (GTX103117), pSTAT1 Y701(7649S), TFE3 (HPA023881), H3 (9715S), Tubulin (B-5-1-2, SC-23948), p70S6Kinase T389 (CST 9205), pAKT S473 D9E (CST 4060), total p70S6K (49D7 CST 2708), panAKT 40D4 (CST 2920), 4E-BP1 53H11 (CST 9644), GAPDH (sc-47724) and (MAB374; Merck Millipore).

Growth curve modeling

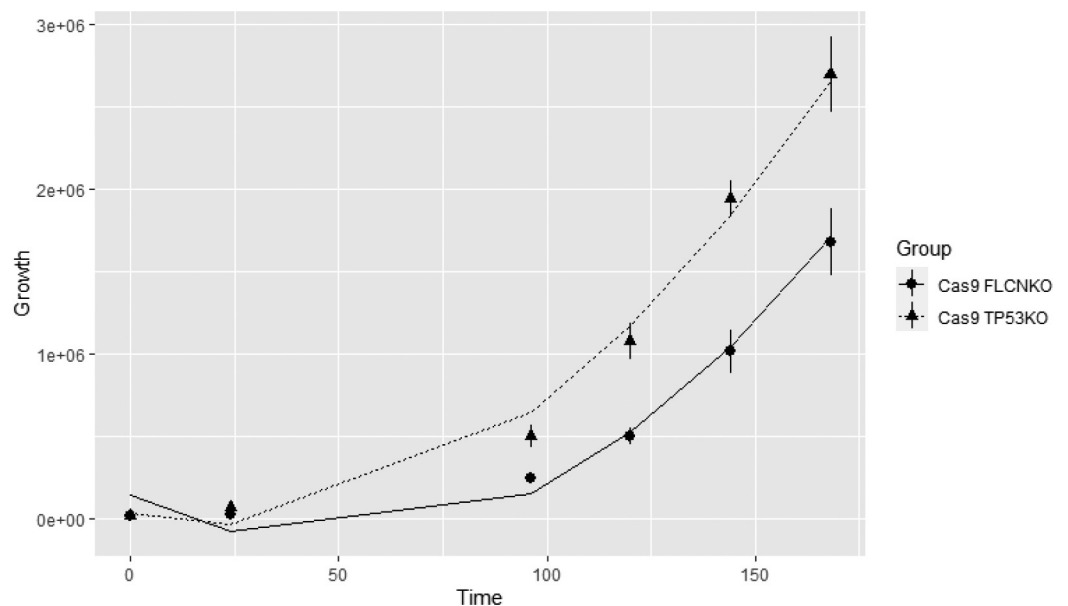
We modeled the growth curve data with a random intercept model (Mirman, 2016; Molenberghs and Verbeke, 2000):

$$Y_{ijk} = (\beta_0 + b_0) + \beta_1 \times \text{Time}_k + \beta_2 \times \text{Time}_k^2 + \beta_3 \times I_{\text{TP53},i} + \beta_4 \times (\text{Time}_k \times I_{\text{TP53},i}) + \varepsilon_{ijk}$$

with Y_{ijk} the number of cells of knock-out j at time k , $I_{\text{TP53},j}$ a binary variable indicating if the i^{th} observation is coming from the Cas9-TP53^{KO} ($I_{\text{TP53},j} = 1$) or from the Cas9-FLCN^{KO} ($I_{\text{TP53},j} = 0$), $b_0 \sim N(0, \sigma_b^2)$, and $\varepsilon_{ijk} \sim N(0, \sigma_\varepsilon^2)$. **Scheme 1** shows the modeled growth curves for both knock-outs.

Based on the estimated values of the random intercept model (**Table 1**), we can conclude that there is a statistically significant difference ($\alpha = 0.05$) in the growth curves of Cas9-FLCN^{KO} and Cas9-TP53^{KO} ($\beta_4 \neq 0$; p-value << 0.05), and that there is a statistically significant increase in the number of cells over time ($\beta_1 \neq 0$; p-value << 0.05; and $\beta_2 \neq 0$; p-value << 0.05).

Scheme 1: Growth rates of FLCNKO and TP53KO cells with fitted curves



Scheme 1. Growth curves of FLCNKO and TP53KO with the fitted curves.

Table 1. Estimated values and p-value of the random intercept model.

	Estimate	Standard error	p-Value
β_0 (FLCN ^{KO} at time 0)	1.414×10^5	1.079×10^5	0.215
β_1 (Time)	-1.222×10^4	1.966×10^3	5.07×10^{-10}
β_2 (Time ²)	1.284×10^2	1.138×10^1	$<2 \times 10^{-16}$
β_3 (TP53 ^{KO})	-1.080×10^5	1.462×10^5	0.477
(interaction between Time and TP53 ^{KO})	6.262×10^3	9.641×10^2	8.31×10^{-11}
σ_b^2	1.506×10^{10}		
σ_ε^2	6.238×10^{10}		

Cytometric bead array and enzyme-linked immunosorbent assay (ELISA)

To detect IFN γ in supernatants, the Human IFN- γ Flex Set (560111, BD Biosciences, Franklin Lakes, New Jersey, USA) was used according to the manual for the BD CBA Human Soluble Protein Master Buffer Kit. Measurements were done on BD LSRFortessa Flow Cytometer (BD Biosciences) and FCAP Array Software. Supernatants were measured twice in duplicate. For detection of IFN α in supernatants, the VeriKine-HS Human IFN- α All Subtype ELISA kit (#41115, PBL assay science, Piscataway, New Jersey, USA) was used according to manufacturer's protocol. For calculation of IFN α concentrations, blank optical densities were subtracted from standard and sample optical densities. Supernatants were measured twice in duplicate.

Clonogenic assays

To assess clonogenicity a Crystal Violet (CV) staining was performed. Cell lines were plated in three technical replicates in a six-well plate at low concentration (3000 cells/well). Plates were incubated in a humidified atmosphere at 37°C and 5% CO₂ for approximately 10 days until plates displayed colonies with substantially good size. At that moment, cells were fixed with ice-cold methanol (Methanol $\geq 99.8\%$, Sigma-Aldrich) and plates were incubated for 5 min at RT after which cells were washed with PBS and stained with CV (0.05% solution, Merck) for 30 min at RT. Then CV was washed away with tap water, plates were air dried and scanned for further analysis. Detail photographs ($\times 20$) were obtained with AxioScope microscope camera and corresponding software (AxioVision SE64 Rel. 4.9.1, Carl Zeiss, Jena, Germany). At least, two independent experiments with three technical replicates were used to determine colony formation capacities.

Acknowledgements

We thank the Core Facility Genomics and in particular Daoud Sie for RNA seq and data analysis; we thank Tanja de Gruijl and Ferenc Scheeren for advice and critically reading the manuscript, and Maurice van Steensel and Jeroen van Moorselaar for fruitful discussions. We thank Irene Bijnsdorp for help with mass spec of tissue material and Jürgen Claesen for assistance with statistical analyses. The authors declare that they have no conflicts of interest with the contents of this article.

Additional information

Funding

Funder	Grant reference number	Author
KWF Kankerbestrijding	Alpe d'Huzes Bas Mulder Award	Jarno Drost
Stichting Kinderen Kankervrij	Core Funding	Sepide Derakhshan
Oncode Institute		Jarno Drost
Cancer Center Amsterdam	CCA2018-5-51	Iris E Glykofridis Rob MF Wolthuis

Cancer Center Amsterdam Core Funding Mass Jaco C Knol
Spectrometry Infrastructure Thang V Pham
Sander R Piersma
Connie R Jimenez

The funders had no role in study design, data collection and interpretation, or the decision to submit the work for publication.

Author contributions

Iris E Glykofridis, Conceptualization, Resources, Data curation, Formal analysis, Validation, Investigation, Visualization, Methodology, Writing - original draft, Project administration, Writing - review and editing; Jaco C Knol, Resources, Data curation, Formal analysis, Visualization, Writing-review and editing; Jesper A Balk, Resources, Validation, Investigation; Denise Westland, Sinéad M Loughheed, Validation, Investigation; Thang V Pham, Resources, Data curation, Formal analysis; Sander R Piersma, Resources, Data curation; Sepide Derakhshan, Resources; Puck Veen, Martin A Rooimans, Saskia E van Mil, Pino J Poddighe, Investigation; Franziska Böttger, Visualization, Methodology; Irma van de Beek, Conceptualization, Methodology, Writing - review and editing; Jarno Drost, Resources, Supervision; Fried JT Zwartkruis, Conceptualization, Supervision, Investigation, Visualization, Writing - review and editing; Renee X de Menezes, Resources, Formal analysis, Methodology; Hanne EJ Meijers-Heijboer, Conceptualization, Supervision, Funding acquisition, Writing - review and editing; Arjan C Houweling, Connie R Jimenez, Conceptualization, Supervision, Funding acquisition, Methodology, Writing - review and editing; Rob MF Wolthuis, Conceptualization, Supervision, Funding acquisition, Methodology, Writing - original draft, Project administration, Writing - review and editing

Author ORCIDs

Iris E Glykofridis  <https://orcid.org/0000-0003-1829-2403>

Rob MF Wolthuis  <https://orcid.org/0000-0002-3109-1588>

Ethics

Human subjects: BHD T1 and BHD T2 tumor samples were obtained with informed consent. Both tissues are leftover material from surgery and are stored in our BHD biobank (2019.359 at AmsterdamUMC).

Decision letter and Author response

Decision letter <https://doi.org/10.7554/eLife.61630.sa1>

Author response <https://doi.org/10.7554/eLife.61630.sa2>

Additional files

Supplementary files

- Supplementary file 1. Table showing differential expression analyses of FLCN^{POS} versus FLCN^{NEG} RPTECs on RNA and protein level.
- Supplementary file 2. Table showing subset of TFE3 targets upregulated in FLCN^{NEG} RPTEC (cluster 3, boxed yellow in **Figure 3A**).
- Transparent reporting form

Data availability

Data files of transcriptomic and proteomic data are provided as Supplementary file 1. Raw data files deposited on Dryad Digital Repository (RNAseq): <https://doi.org/10.5061/dryad.6djh9w0zs> and Mass Spec Data are deposited on ProteomeXchange (Mass Spec) under accession number PXD021346.

The following datasets were generated:

Author(s)	Year	Dataset title	Dataset URL	Database and Identifier
Glykofridis IE, Wolthuis RM	2021	RNAseq raw counts_FLCN positive vs. FLCN negative RPTECs	http://dx.doi.org/10.5061/dryad.6djh9w0zs	Dryad Digital Repository, 10.5061/dryad.6djh9w0zs
Piersma SR, Jimenez CR	2021	Loss of FLCN-FNIP1/2 Induces a Non-Canonical Interferon 1 Response in Human Renal Tubular Epithelial Cells	https://www.ebi.ac.uk/pride/archive/projects/PXD021346	PRIDE, PXD021346

References

- Ambalavanan M**, Geller JI. 2019. Treatment of advanced pediatric renal cell carcinoma. *Pediatric Blood & Cancer* **66**:e27766. DOI: <https://doi.org/10.1002/pbc.27766>, PMID: 31012542
- Aschauer L**, Limonciel A, Wilmes A, Stanzel S, Kopp-Schneider A, Hewitt P, Lukas A, Leonard MO, Pfaller W, Jennings P. 2015. Application of RPTEC/TERT1 cells for investigation of repeat dose nephrotoxicity: a transcriptomic study. *Toxicology in Vitro* **30**:106–116. DOI: <https://doi.org/10.1016/j.tiv.2014.10.005>, PMID: 25450743
- Baba M**, Hong SB, Sharma N, Warren MB, Nickerson ML, Iwamatsu A, Esposito D, Gillette WK, Hopkins RF, Hartley JL, Furihata M, Oishi S, Zhen W, Burke TR, Linehan WM, Schmidt LS, Zbar B. 2006. Folliculin encoded by the BHD gene interacts with a binding protein, FNIP1, and AMPK, and is involved in AMPK and mTOR signaling. *PNAS* **103**:15552–15557. DOI: <https://doi.org/10.1073/pnas.0603781103>, PMID: 17028174
- Bastola P**, Stratton Y, Kellner E, Mikhaylova O, Yi Y, Sartor MA, Medvedovic M, Biesiada J, Meller J, Czyzyk-Krzeska MF. 2013. Folliculin contributes to VHL tumor suppressing activity in renal Cancer through regulation of autophagy. *PLOS ONE* **8**:e70030. DOI: <https://doi.org/10.1371/journal.pone.0070030>, PMID: 23922894
- Bedford JJ**, Leader JP, Walker RJ. 2003. Aquaporin expression in normal human kidney and in renal disease. *Journal of the American Society of Nephrology* **14**:2581–2587. DOI: <https://doi.org/10.1097/01.ASN.0000089566.28106.F6>, PMID: 14514735
- Bektas N**, Noetzel E, Veeck J, Press MF, Kristiansen G, Naami A, Hartmann A, Dimmler A, Beckmann MW, Knüchel R, Fasching PA, Dahl E. 2008. The ubiquitin-like molecule interferon-stimulated gene 15 (ISG15) is a potential prognostic marker in human breast Cancer. *Breast Cancer Research* **10**:R58. DOI: <https://doi.org/10.1186/bcr2117>, PMID: 18627608
- Benedict B**, van Schie JJM, Oostra AB, Balk JA, Wolthuis RMF, Riele HT, de Lange J. 2020. WAPL-Dependent repair of damaged DNA replication forks underlies Oncogene-Induced loss of sister chromatid cohesion. *Developmental Cell* **52**:683–698. DOI: <https://doi.org/10.1016/j.devcel.2020.01.024>, PMID: 32084359
- Benjamini Y**, Hochberg Y. 1995. Controlling the false discovery rate: a practical and powerful approach to multiple testing. *Journal of the Royal Statistical Society: Series B* **57**:289–300. DOI: <https://doi.org/10.1111/j.2517-6161.1995.tb02031.x>
- Betschinger J**, Nichols J, Dietmann S, Corrin PD, Paddison PJ, Smith A. 2013. Exit from pluripotency is gated by intracellular redistribution of the bHLH transcription factor Tfe3. *Cell* **153**:335–347. DOI: <https://doi.org/10.1016/j.cell.2013.03.012>, PMID: 23582324
- Birt AR**, Hogg GR, Dubé WJ. 1977. Hereditary multiple fibrofolliculomas with trichodiscomas and acrochordons. *Archives of Dermatology* **113**:1674–1677. DOI: <https://doi.org/10.1001/archderm.1977.01640120042005>, PMID: 596896
- Calandrini C**, Schutgens F, Oka R, Margaritis T, Candelli T, Mathijssen L, Ammerlaan C, van Ineveld RL, Derakhshan S, de Haan S, Dolman E, Lijnzaad P, Custers L, Begthel H, Kerstens HHD, Visser LL, Rookmaaker M, Verhaar M, Tytgat GAM, Kemmeren P, et al. 2020. An organoid biobank for childhood kidney cancers that captures disease and tissue heterogeneity. *Nature Communications* **11**:1310. DOI: <https://doi.org/10.1038/s41467-020-15155-6>, PMID: 32161258
- Caliò A**, Segala D, Munari E, Brunelli M, Martignoni G. 2019. MiT family translocation renal cell carcinoma: from the early descriptions to the current knowledge. *Cancers* **11**:1110. DOI: <https://doi.org/10.3390/cancers11081110>
- Chen J**, Futami K, Petillo D, Peng J, Wang P, Knol J, Li Y, Khoo SK, Huang D, Qian CN, Zhao P, Dykema K, Dykema K, Zhang R, Cao B, Yang XJ, Furge K, Williams BO, Teh BT. 2008. Deficiency of FLCN in mouse kidney led to development of polycystic kidneys and renal neoplasia. *PLOS ONE* **3**:e3581. DOI: <https://doi.org/10.1371/journal.pone.0003581>, PMID: 18974783
- Chen J**, Huang D, Rubera I, Futami K, Wang P, Zickert P, Khoo SK, Dykema K, Zhao P, Petillo D, Cao B, Zhang Z, Si S, Schoen SR, Yang XJ, Zhou M, Xiao GQ, Wu G, Nordenskjöld M, Tauc M, et al. 2015. Disruption of tubular flcn expression as a mouse model for renal tumor induction. *Kidney International* **88**:1057–1069. DOI: <https://doi.org/10.1038/ki.2015.177>, PMID: 26083655
- De Zan E**, van Stiphout R, Gapp BV, Blomen VA, Brummelkamp TR, Nijman SMB. 2020. Quantitative genetic screening reveals a Ragulator-FLCN feedback loop that regulates the mTORC1 pathway. *Science Signaling* **13**:eaba5665. DOI: <https://doi.org/10.1126/scisignal.aba5665>, PMID: 32934076
- Di Malta C**, Siciliano D, Calcagni A, Monfregola J, Punzi S, Pastore N, Eastes AN, Davis O, De Cegli R, Zampelli A, Di Giovannantonio LG, Nusco E, Platt N, Guida A, Ogmundsdottir MH, Lanfrancone L, Perera RM, Zoncu R,

- Pelicci PG, Settembre C, et al. 2017. Transcriptional activation of RagD GTPase controls mTORC1 and promotes Cancer growth. *Science* **356**:1188–1192. DOI: <https://doi.org/10.1126/science.aag2553>, PMID: 28619945
- Dunlop EA, Seifan S, Claessens T, Behrends C, Kamps MA, Rozycka E, Kemp AJ, Nookala RK, Blenis J, Coull BJ, Murray JT, van Steensel MA, Wilkinson S, Tee AR. 2014. FLCN, a novel autophagy component, interacts with GABARAP and is regulated by ULK1 phosphorylation. *Autophagy* **10**:1749–1760. DOI: <https://doi.org/10.4161/aut.29640>, PMID: 25126726
- El-Houjeiri L, Possik E, Vijayaraghavan T, Paquette M, Martina JA, Kazan JM, Ma EH, Jones R, Blanchette P, Puertollano R, Pause A. 2019. The transcription factors TFEB and TFE3 link the FLCN-AMPK signaling Axis to innate immune response and pathogen resistance. *Cell Reports* **26**:3613–3628. DOI: <https://doi.org/10.1016/j.celrep.2019.02.102>, PMID: 30917316
- Endoh M, Baba M, Endoh T, Hirayama A, Nakamura-Ishizu A, Umemoto T, Hashimoto M, Nagashima K, Soga T, Lang M, Schmidt LS, Linehan WM, Suda T. 2020. A FLCN-TFE3 feedback loop prevents excessive glycogenesis and phagocyte activation by regulating lysosome activity. *Cell Reports* **30**:1823–1834. DOI: <https://doi.org/10.1016/j.celrep.2020.01.042>
- Farmer G, Bargonetti J, Zhu H, Friedman P, Prywes R, Prives C. 1992. Wild-type p53 activates transcription in vitro. *Nature* **358**:83–86. DOI: <https://doi.org/10.1038/358083a0>, PMID: 1614538
- Ferlay J, Colombet M, Soerjomataram I, Mathers C, Parkin DM, Piñeros M, Znaor A, Bray F. 2019. Estimating the global Cancer incidence and mortality in 2018: globocan sources and methods. *International Journal of Cancer* **144**:1941–1953. DOI: <https://doi.org/10.1002/ijc.31937>, PMID: 30350310
- Fields S, Jang SK. 1990. Presence of a potent transcription activating sequence in the p53 protein. *Science* **249**:1046–1049. DOI: <https://doi.org/10.1126/science.2144363>, PMID: 2144363
- Fratantoni SA, Piersma SR, Jimenez CR. 2010. Comparison of the performance of two affinity depletion spin filters for quantitative proteomics of CSF: evaluation of sensitivity and reproducibility of CSF analysis using GeLC-MS/MS and spectral counting. *Proteomics - Clinical Applications* **4**:613–617. DOI: <https://doi.org/10.1002/prca.200900179>, PMID: 21137079
- Fumagalli A, Drost J, Suijkerbuijk SJ, van Boxtel R, de Ligt J, Offerhaus GJ, Begthel H, Beerling E, Tan EH, Sansom OJ, Cuppen E, Clevers H, van Rheenen J. 2017. Genetic dissection of colorectal Cancer progression by orthotopic transplantation of engineered Cancer organoids. *PNAS* **114**:E2357–E2364. DOI: <https://doi.org/10.1073/pnas.1701219114>, PMID: 28270604
- Grant A, Ponia SS, Tripathi S, Balasubramaniam V, Miorin L, Sourisseau M, Schwarz MC, Sánchez-Seco MP, Evans MJ, Best SM, García-Sastre A. 2016. Zika virus targets human STAT2 to inhibit type I interferon signaling. *Cell Host & Microbe* **19**:882–890. DOI: <https://doi.org/10.1016/j.chom.2016.05.009>, PMID: 27212660
- Haapaniemi E, Botla S, Persson J, Schmierer B, Taipale J. 2018. CRISPR-Cas9 genome editing induces a p53-mediated DNA damage response. *Nature Medicine* **24**:927–930. DOI: <https://doi.org/10.1038/s41591-018-0049-z>, PMID: 29892067
- Hartman TR, Nicolas E, Klein-Szanto A, Al-Saleem T, Cash TP, Simon MC, Henske EP. 2009. The role of the Birt-Hogg-Dubé protein in mTOR activation and renal tumorigenesis. *Oncogene* **28**:1594–1604. DOI: <https://doi.org/10.1038/onc.2009.14>, PMID: 19234517
- Hasumi H, Baba M, Hong SB, Hasumi Y, Huang Y, Yao M, Valera VA, Linehan WM, Schmidt LS. 2008. Identification and characterization of a novel folliculin-interacting protein FNI2. *Gene* **415**:60–67. DOI: <https://doi.org/10.1016/j.gene.2008.02.022>, PMID: 18403135
- Hasumi Y, Baba M, Ajima R, Hasumi H, Valera VA, Klein ME, Haines DC, Merino MJ, Hong SB, Yamaguchi TP, Schmidt LS, Linehan WM. 2009. Homozygous loss of BHD causes early embryonic lethality and kidney tumor development with activation of mTORC1 and mTORC2. *PNAS* **106**:18722–18727. DOI: <https://doi.org/10.1073/pnas.0908853106>, PMID: 19850877
- Hasumi H, Baba M, Hasumi Y, Huang Y, Oh H, Hughes RM, Klein ME, Takikita S, Nagashima K, Schmidt LS, Linehan WM. 2012. Regulation of mitochondrial oxidative metabolism by tumor suppressor FLCN. *JNCI: Journal of the National Cancer Institute* **104**:1750–1764. DOI: <https://doi.org/10.1093/jnci/djs418>
- Hasumi H, Baba M, Hasumi Y, Lang M, Huang Y, Oh HF, Matsuo M, Merino MJ, Yao M, Ito Y, Furuya M, Iribe Y, Kodama T, Southon E, Tessarollo L, Nagashima K, Haines DC, Linehan WM, Schmidt LS. 2015. Folliculin-interacting proteins Fni1 and Fni2 play critical roles in kidney tumor suppression in cooperation with flcn. *PNAS* **112**:E1624–E1631. DOI: <https://doi.org/10.1073/pnas.1419502112>, PMID: 25775561
- Holthöfer H, Miettinen A, Paasivuo R, Lehto VP, Linder E, Alfthan O, Virtanen I. 1983. Cellular origin and differentiation of renal carcinomas. A fluorescence microscopic study with kidney-specific antibodies, antiintermediate filament antibodies, and lectins. *Laboratory Investigation; a Journal of Technical Methods and Pathology* **49**:317–326. PMID: 6193332
- Hong S-B, Oh H, Valera VA, Baba M, Schmidt LS, Linehan WM. 2010a. Inactivation of the FLCN tumor suppressor gene induces TFE3 transcriptional activity by increasing its nuclear localization. *PLOS ONE* **5**:e15793. DOI: <https://doi.org/10.1371/journal.pone.0015793>
- Hong SB, Oh H, Valera VA, Stull J, Ngo DT, Baba M, Merino MJ, Linehan WM, Schmidt LS. 2010b. Tumor suppressor FLCN inhibits tumorigenesis of a FLCN-null renal Cancer cell line and regulates expression of key molecules in TGF-beta signaling. *Molecular Cancer* **9**:160. DOI: <https://doi.org/10.1186/1476-4598-9-160>, PMID: 20573232
- Houweling AC, Gijzen LM, Jonker MA, van Doorn MB, Oldenburg RA, van Spaendonck-Zwarts KY, Leter EM, van Os TA, van Grieken NC, Jaspars EH, de Jong MM, Bongers EM, Johannesma PC, Postmus PE, van Moorselaar RJ, van Waesberghe JH, Starink TM, van Steensel MA, Gille JJ, Menko FH. 2011. Renal Cancer and

- pneumothorax risk in Birt-Hogg-Dubé syndrome; an analysis of 115 FLCN mutation carriers from 35 BHD families. *British Journal of Cancer* **105**:1912–1919. DOI: <https://doi.org/10.1038/bjc.2011.463>, PMID: 22146830
- Hudon V**, Sabourin S, Dydensborg AB, Kottis V, Ghazi A, Paquet M, Crosby K, Pomerleau V, Uetani N, Pause A. 2010. Renal tumour suppressor function of the Birt-Hogg-Dubé syndrome gene product folliculin. *Journal of Medical Genetics* **47**:182–189. DOI: <https://doi.org/10.1136/jmg.2009.072009>, PMID: 19843504
- Ihry RJ**, Worringer KA, Salick MR, Frias E, Ho D, Theriault K, Kommineni S, Chen J, Sondey M, Ye C, Randhawa R, Kulkarni T, Yang Z, McAllister G, Russ C, Reece-Hoyes J, Forrester W, Hoffman GR, Dolmetsch R, Kaykas A. 2018. p53 inhibits CRISPR-Cas9 engineering in human pluripotent stem cells. *Nature Medicine* **24**:939–946. DOI: <https://doi.org/10.1038/s41591-018-0050-6>, PMID: 29892062
- Illumina I**. 2020. iGenomes resource. https://emea.support.illumina.com/sequencing/sequencing_software/igenome.html [Accessed June 1, 2020].
- Janky R**, Verfaillie A, Imrichová H, Van de Sande B, Standaert L, Christiaens V, Hulselmans G, Herten K, Naval Sanchez M, Potier D, Svetlichnyy D, Kalender Atak Z, Fiers M, Marine JC, Aerts S. 2014. iRegulon: from a gene list to a gene regulatory network using large motif and track collections. *PLOS Computational Biology* **10**:e1003731. DOI: <https://doi.org/10.1371/journal.pcbi.1003731>, PMID: 25058159
- Johannesma PC**, van de Beek I, van der Wel T, Reinhard R, Rozendaal L, Starink TM, van Waesberghe J, Horenblas S, Gille H, Jonker MA, Meijers-Heijboer HEJ, Postmus PE, Houweling AC, van Moorselaar JRA. 2019. Renal imaging in 199 dutch patients with Birt-Hogg-Dubé syndrome: screening compliance and outcome. *PLOS ONE* **14**:e0212952. DOI: <https://doi.org/10.1371/journal.pone.0212952>, PMID: 30845233
- Joshi N**, Fass J. 2011. Sickie: A Sliding-Window, Adaptive, Quality-Based Trimming Tool for FastQ Files. *GitHub*. 1.33. <https://github.com/najoshi/sickle>
- Kardas I**, Mrózek K, Babinska M, Krajka K, Hadaczek P, Lubinski J, Roszkiewicz A, Kuziemska E, Limon J. 2005. Cytogenetic and molecular findings in 75 clear cell renal cell carcinomas. *Oncology Reports* **13**:949–956. DOI: <https://doi.org/10.3892/or.13.5.949>, PMID: 15809763
- Khabibullin D**, Medvetz DA, Pinilla M, Hariharan V, Li C, Hergueter A, Laucho Contreras M, Zhang E, Parkhitko A, Yu JJ, Owen CA, Huang H, Baron RM, Henske EP. 2014. Folliculin regulates cell-cell adhesion, AMPK, and mTORC1 in a cell-type-specific manner in lung-derived cells. *Physiological Reports* **2**:e12107. DOI: <https://doi.org/10.14814/phy2.12107>, PMID: 25121506
- Kim D**, Langmead B, Salzberg SL. 2015. HISAT: a fast spliced aligner with low memory requirements. *Nature Methods* **12**:357–360. DOI: <https://doi.org/10.1038/nmeth.3317>, PMID: 25751142
- Labbé C**, Boucher G, Foisy S, Alikashani A, Nkwimi H, David G, Beaudoin M, Goyette P, Charron G, Xavier RJ, Rioux JD. 2012. Genome-wide expression profiling implicates a MAST3-regulated gene set in colonic mucosal inflammation of ulcerative colitis patients. *Inflammatory Bowel Diseases* **18**:1072–1080. DOI: <https://doi.org/10.1002/ibd.21887>, PMID: 21994190
- Laviolette LA**, Wilson J, Koller J, Neil C, Hulick P, Rejtar T, Karger B, Teh BT, Iliopoulos O. 2013. Human folliculin delays cell cycle progression through late S and G2/M-phases: effect of phosphorylation and tumor associated mutations. *PLOS ONE* **8**:e66775. DOI: <https://doi.org/10.1371/journal.pone.0066775>, PMID: 23874397
- Lee HJ**, Shin DH, Kim SY, Hwang CS, Lee JH, Park WY, Choi KU, Kim JY, Lee CH, Sol MY, Rha SH, Park SW. 2018. TFE3 translocation and protein expression in renal cell carcinoma are correlated with poor prognosis. *Histopathology* **73**:758–766. DOI: <https://doi.org/10.1111/his.13700>, PMID: 29968390
- Liao Y**, Smyth GK, Shi W. 2014. featureCounts: an efficient general purpose program for assigning sequence reads to genomic features. *Bioinformatics* **30**:923–930. DOI: <https://doi.org/10.1093/bioinformatics/btt656>, PMID: 24227677
- Liberzon A**, Subramanian A, Pinchback R, Thorvaldsdóttir H, Tamayo P, Mesirov JP. 2011. Molecular signatures database (MSigDB) 3.0. *Bioinformatics* **27**:1739–1740. DOI: <https://doi.org/10.1093/bioinformatics/btr260>, PMID: 21546393
- Liu H**, Sadygov RG, Yates JR. 2004. A model for random sampling and estimation of relative protein abundance in shotgun proteomics. *Analytical Chemistry* **76**:4193–4201. DOI: <https://doi.org/10.1021/ac0498563>, PMID: 15253663
- Lopez-Beltran A**, Scarpelli M, Montironi R, Kirkali Z. 2006. 2004 WHO classification of the renal tumors of the adults. *European Urology* **49**:798–805. DOI: <https://doi.org/10.1016/j.eururo.2005.11.035>, PMID: 16442207
- Luijten MN**, Basten SG, Claessens T, Vernooij M, Scott CL, Janssen R, Easton JA, Kamps MA, Vreeburg M, Broers JL, van Geel M, Menko FH, Harbottle RP, Nookala RK, Tee AR, Land SC, Giles RH, Coull BJ, van Steensel MA. 2013. Birt-Hogg-Dubé syndrome is a novel ciliopathy. *Human Molecular Genetics* **22**:4383–4397. DOI: <https://doi.org/10.1093/hmg/ddt288>, PMID: 23784378
- Maere S**, Heymans K, Kuiper M. 2005. BiNGO: a cytoscape plugin to assess overrepresentation of gene ontology categories in biological networks. *Bioinformatics* **21**:3448–3449. DOI: <https://doi.org/10.1093/bioinformatics/bti551>, PMID: 15972284
- Majoros A**, Platanitis E, Kernbauer-Hözl E, Rosebrock F, Müller M, Decker T. 2017. Canonical and Non-Canonical aspects of JAK-STAT signaling: lessons from interferons for cytokine responses. *Frontiers in Immunology* **8**:29. DOI: <https://doi.org/10.3389/fimmu.2017.00029>, PMID: 28184222
- Martina JA**, Diab HI, Li H, Puertollano R. 2014. Novel roles for the MITF/TFE family of transcription factors in organelle biogenesis, nutrient sensing, and energy homeostasis. *Cellular and Molecular Life Sciences* **71**:2483–2497. DOI: <https://doi.org/10.1007/s00018-014-1565-8>, PMID: 24477476
- Mathieu J**, Detraux D, Kuppers D, Wang Y, Cavanaugh C, Sidhu S, Robitaille AM, Ferreccio A, Bottorff T, McAlister A, Somasundaram L, Artoni F, Battle S, Hawkins RD, Moon RT, Ware CB, Paddison PJ, Ruohola-Baker

- H. 2019. Folliculin regulates mTORC1/2 and WNT pathways in early human pluripotency. *Nature Communications* **10**:632. DOI: <https://doi.org/10.1038/s41467-018-08020-0>, PMID: 30733432
- McGowan-Jordan J, Simons A, Schmid M. 2016. *ISCN 2016: An International System for Human Cytogenetic Nomenclature*. Basel: Karger.
- Mirman D. 2016. *Growth Curve Analysis and Visualization Using R*. CRC press. DOI: <https://doi.org/10.18637/jss.v058.b02>
- Molenberghs G, Verbeke G. 2000. *Linear Mixed Models for Longitudinal Data*. Springer. DOI: <https://doi.org/10.1007/978-1-4419-0300-6>
- Morlote DM, Harada S, Batista D, Gordetsky J, Rais-Bahrami S. 2019. Clear cell papillary renal cell carcinoma: molecular profile and virtual karyotype. *Human Pathology* **91**:52–60. DOI: <https://doi.org/10.1016/j.humpath.2019.05.011>, PMID: 31175917
- Morrison J, Miorin L, Laurent-Rolle M, Pisanelli G, Co P, Albrecht R, García-Sastre A. 2019. STAT2 is a determinant of yellow fever virus host tropism. *The Journal of Immunology* **202**:127.
- Nahorski MS, Reiman A, Lim DH, Nookala RK, Seabra L, Lu X, Fenton J, Boora U, Nordenskjöld M, Latif F, Hurst LD, Maher ER. 2011. Birt Hogg-Dubé syndrome-associated FLCN mutations disrupt protein stability. *Human Mutation* **32**:921–929. DOI: <https://doi.org/10.1002/humu.21519>, PMID: 21538689
- Napolitano G, Di Malta C, Esposito A, de Araujo MEG, Pece S, Bertalot G, Matarese M, Benedetti V, Zampelli A, Stasyk T, Siciliano D, Venuta A, Cesana M, Vilaro C, Nusco E, Monfregola J, Calcagni A, Di Fiore PP, Huber LA, Ballabio A. 2020. A substrate-specific mTORC1 pathway underlies Birt-Hogg-Dubé syndrome. *Nature* **585**:597–602. DOI: <https://doi.org/10.1038/s41586-020-2444-0>, PMID: 32612235
- Nepusz T, Yu H, Paccanaro A. 2012. Detecting overlapping protein complexes in protein-protein interaction networks. *Nature Methods* **9**:471–472. DOI: <https://doi.org/10.1038/nmeth.1938>, PMID: 22426491
- Nickerson ML, Warren MB, Toro JR, Matrosova V, Glenn G, Turner ML, Duray P, Merino M, Choyke P, Pavlovich CP, Sharma N, Walther M, Munroe D, Hill R, Maher E, Greenberg C, Lerman MI, Linehan WM, Zbar B, Schmidt LS. 2002. Mutations in a novel gene lead to kidney tumors, lung wall defects, and benign tumors of the hair follicle in patients with the Birt-Hogg-Dubé syndrome. *Cancer Cell* **2**:157–164. DOI: [https://doi.org/10.1016/S1535-6108\(02\)00104-6](https://doi.org/10.1016/S1535-6108(02)00104-6), PMID: 12204536
- Nookala RK, Langemeyer L, Pacitto A, Ochoa-Montaña B, Donaldson JC, Blaszczyk BK, Chirgadze DY, Barr FA, Bazan JF, Blundell TL. 2012. Crystal structure of folliculin reveals a hidDENN function in genetically inherited renal cancer. *Open Biology* **2**:120071. DOI: <https://doi.org/10.1098/rsob.120071>
- Pacitto A, Ascher DB, Wong LH, Blaszczyk BK, Nookala RK, Zhang N, Dokudovskaya S, Levine TP, Blundell TL. 2015. Lst4, the yeast Fnp1/2 orthologue, is a DENN-family protein. *Open Biology* **5**:150174. DOI: <https://doi.org/10.1098/rsob.150174>, PMID: 26631379
- Palmieri M, Impey S, Kang H, di Ronza A, Pelz C, Sardiello M, Ballabio A. 2011. Characterization of the CLEAR network reveals an integrated control of cellular clearance pathways. *Human Molecular Genetics* **20**:3852–3866. DOI: <https://doi.org/10.1093/hmg/ddr306>, PMID: 21752829
- Pavlovich CP, Grubb RL, Hurley K, Glenn GM, Toro J, Schmidt LS, Torres-Cabala C, Merino MJ, Zbar B, Choyke P, Walther MM, Linehan WM. 2005. Evaluation and management of renal tumors in the birt-hogg-dubé syndrome. *Journal of Urology* **173**:1482–1486. DOI: <https://doi.org/10.1097/01.ju.0000154629.45832.30>
- Petit CS, Roczniak-Ferguson A, Ferguson SM. 2013. Recruitment of folliculin to lysosomes supports the amino acid-dependent activation of Rag GTPases. *Journal of Cell Biology* **202**:1107–1122. DOI: <https://doi.org/10.1083/jcb.201307084>
- Pham TV, Piersma SR, Warmoes M, Jimenez CR. 2010. On the beta-binomial model for analysis of spectral count data in label-free tandem mass spectrometry-based proteomics. *Bioinformatics* **26**:363–369. DOI: <https://doi.org/10.1093/bioinformatics/btp677>, PMID: 20007255
- Piersma SR, Fiedler U, Span S, Lingnau A, Pham TV, Hoffmann S, Kubbutat MH, Jiménez CR. 2010. Workflow comparison for label-free, quantitative secretome proteomics for Cancer biomarker discovery: method evaluation, differential analysis, and verification in serum. *Journal of Proteome Research* **9**:1913–1922. DOI: <https://doi.org/10.1021/pr901072h>, PMID: 20085282
- Piersma SR, Warmoes MO, de Wit M, de Reus I, Knol JC, Jiménez CR. 2013. Whole gel processing procedure for GeLC-MS/MS based proteomics. *Proteome Science* **11**:17. DOI: <https://doi.org/10.1186/1477-5956-11-17>, PMID: 23617947
- Possik E, Jalali Z, Nouët Y, Yan M, Gingras MC, Schmeisser K, Panaite L, Dupuy F, Kharitidi D, Chotard L, Jones RG, Hall DH, Pause A. 2014. Folliculin regulates ampk-dependent autophagy and metabolic stress survival. *PLOS Genetics* **10**:e1004273. DOI: <https://doi.org/10.1371/journal.pgen.1004273>, PMID: 24763318
- Preston RS, Philp A, Claessens T, Gijzen L, Dydensborg AB, Dunlop EA, Harper KT, Brinkhuizen T, Menko FH, Davies DM, Land SC, Pause A, Baar K, van Steensel MA, Tee AR. 2011. Absence of the Birt-Hogg-Dubé gene product is associated with increased hypoxia-inducible factor transcriptional activity and a loss of metabolic flexibility. *Oncogene* **30**:1159–1173. DOI: <https://doi.org/10.1038/onc.2010.497>, PMID: 21057536
- Puleo JI, Parker SS, Roman MR, Watson AW, Eliato KR, Peng L, Saboda K, Roe DJ, Ros R, Gertler FB, Mouneimne G. 2019. Mechanosensing during directed cell migration requires dynamic actin polymerization at focal adhesions. *Journal of Cell Biology* **218**:4215–4235. DOI: <https://doi.org/10.1083/jcb.201902101>
- Robinson MD, McCarthy DJ, Smyth GK. 2010. edgeR: a bioconductor package for differential expression analysis of digital gene expression data. *Bioinformatics* **26**:139–140. DOI: <https://doi.org/10.1093/bioinformatics/btp616>, PMID: 19910308

- Rose AAN, Biondini M, Curiel R, Siegel PM. 2017. Targeting GPNMB with glebatumumab vedotin: current developments and future opportunities for the treatment of Cancer. *Pharmacology & Therapeutics* **179**:127–141. DOI: <https://doi.org/10.1016/j.pharmthera.2017.05.010>, PMID: 28546082
- Santaguida S, Vasile E, White E, Amon A. 2015. Aneuploidy-induced cellular stresses limit autophagic degradation. *Genes & Development* **29**:2010–2021. DOI: <https://doi.org/10.1101/gad.269118.115>, PMID: 26404941
- Schmidt LS, Nickerson ML, Warren MB, Glenn GM, Toro JR, Merino MJ, Turner ML, Choyke PL, Sharma N, Peterson J, Morrison P, Maher ER, Walther MM, Zbar B, Linehan WM. 2005. Germline BHD-mutation spectrum and phenotype analysis of a large cohort of families with Birt-Hogg-Dubé syndrome. *The American Journal of Human Genetics* **76**:1023–1033. DOI: <https://doi.org/10.1086/430842>, PMID: 15852235
- Secker P. 2018. RPTEC/TERT1 cells form highly differentiated tubules when cultured in a 3D matrix. *Altex* **35**: 223–234. DOI: <https://doi.org/10.14573/altex.1710181>
- Shannon P, Markiel A, Ozier O, Baliga NS, Wang JT, Ramage D, Amin N, Schwikowski B, Ideker T. 2003. Cytoscape: a software environment for integrated models of biomolecular interaction networks. *Genome Research* **13**:2498–2504. DOI: <https://doi.org/10.1101/gr.1239303>, PMID: 14597658
- Siegel RL, Miller KD, Jemal A. 2018. Cancer statistics, 2018. *CA: A Cancer Journal for Clinicians* **68**:7–30. DOI: <https://doi.org/10.3322/caac.21442>
- Subramanian A, Tamayo P, Mootha VK, Mukherjee S, Ebert BL, Gillette MA, Paulovich A, Pomeroy SL, Golub TR, Lander ES, Mesirov JP. 2005. Gene set enrichment analysis: a knowledge-based approach for interpreting genome-wide expression profiles. *PNAS* **102**:15545–15550. DOI: <https://doi.org/10.1073/pnas.0506580102>, PMID: 16199517
- Szklarczyk D, Gable AL, Lyon D, Junge A, Wyder S, Huerta-Cepas J, Simonovic M, Doncheva NT, Morris JH, Bork P, Jensen LJ, Mering CV. 2019. STRING v11: protein-protein association networks with increased coverage, supporting functional discovery in genome-wide experimental datasets. *Nucleic Acids Research* **47**: D607–D613. DOI: <https://doi.org/10.1093/nar/gky1131>, PMID: 30476243
- Takagi Y, Kobayashi T, Shiono M, Wang L, Piao X, Sun G, Zhang D, Abe M, Hagiwara Y, Takahashi K, Hino O. 2008. Interaction of folliculin (Birt-Hogg-Dubé gene product) with a novel Fnip1-like (FnipL/Fnip2) protein. *Oncogene* **27**:5339–5347. DOI: <https://doi.org/10.1038/onc.2008.261>, PMID: 18663353
- Taya M, Hammes SR. 2018. Glycoprotein Non-Metastatic melanoma protein B (GPNMB) and Cancer: a novel potential therapeutic target. *Steroids* **133**:102–107. DOI: <https://doi.org/10.1016/j.steroids.2017.10.013>, PMID: 29097143
- Toro JR, Wei MH, Glenn GM, Weinreich M, Toure O, Vocke C, Turner M, Choyke P, Merino MJ, Pinto PA, Steinberg SM, Schmidt LS, Linehan WM. 2008. BHD mutations, clinical and molecular genetic investigations of Birt-Hogg-Dubé syndrome: a new series of 50 families and a review of published reports. *Journal of Medical Genetics* **45**:321–331. DOI: <https://doi.org/10.1136/jmg.2007.054304>, PMID: 18234728
- Tsun Z-Y, Bar-Peled L, Chantranupong L, Zoncu R, Wang T, Kim C, Spooner E, Sabatini DM. 2013. The folliculin tumor suppressor is a GAP for the RagC/D GTPases that signal amino acid levels to mTORC1. *Molecular Cell* **52**:495–505. DOI: <https://doi.org/10.1016/j.molcel.2013.09.016>
- van Steensel MAM, Verstraeten VLRM, Frank J, Kelleners-Smeets NWJ, Poblete-Gutiérrez P, Marcus-Soekarman D, Bladergroen RS, Steijlen PM, van Geel M. 2007. Novel mutations in the BHD gene and absence of loss of heterozygosity in fibrofolliculomas of Birt-Hogg-Dubé patients. *Journal of Investigative Dermatology* **127**:588–593. DOI: <https://doi.org/10.1038/sj.jid.5700592>
- Vocke CD, Yang Y, Pavlovich CP, Schmidt LS, Nickerson ML, Torres-Cabala CA, Merino MJ, Walther MM, Zbar B, Linehan WM. 2005. High frequency of somatic frameshift BHD gene mutations in Birt-Hogg-Dubé-Associated Renal Tumors. *JNCI: Journal of the National Cancer Institute* **97**:931–935. DOI: <https://doi.org/10.1093/jnci/dji154>
- Vogelstein B, Kinzler KW. 1992. p53 function and dysfunction. *Cell* **70**:523–526. DOI: [https://doi.org/10.1016/0092-8674\(92\)90421-8](https://doi.org/10.1016/0092-8674(92)90421-8)
- Wada S, Neinast M, Jang C, Ibrahim YH, Lee G, Babu A, Li J, Hoshino A, Rowe GC, Rhee J, Martina JA, Puertollano R, Blenis J, Morley M, Baur JA, Seale P, Arany Z. 2016. The tumor suppressor FLCN mediates an alternate mTOR pathway to regulate Browning of adipose tissue. *Genes & Development* **30**:2551–2564. DOI: <https://doi.org/10.1101/gad.287953.116>, PMID: 27913603
- Wickham H. 2016. *Ggplot2: Elegant Graphics for Data Analysis*. Springer. DOI: <https://doi.org/10.1007/978-3-319-24277-4>
- Wieser M, Stadler G, Jennings P, Streubel B, Pfaller W, Ambros P, Riedl C, Katinger H, Grillari J, Grillari-Voglauer R. 2008. hTERT alone immortalizes epithelial cells of renal proximal tubules without changing their functional characteristics. *American Journal of Physiology-Renal Physiology* **295**:F1365–F1375. DOI: <https://doi.org/10.1152/ajprenal.90405.2008>, PMID: 18715936
- Yan M, Audet-Walsh E, Manteghi S, Dufour CR, Walker B, Baba M, St-Pierre J, Giguère V, Pause A. 2016. Chronic AMPK activation via loss of FLCN induces functional beige adipose tissue through PGC-1 α /ERR α . *Genes & Development* **30**:1034–1046. DOI: <https://doi.org/10.1101/gad.281410.116>
- Yang Y, Padilla-Nash HM, Vira MA, Abu-Asab MS, Val D, Worrell R, Tsokos M, Merino MJ, Pavlovich CP, Riedl T, Linehan WM, Vocke CD. 2008. The UOK 257 cell line: a novel model for studies of the human Birt-Hogg-Dubé gene pathway. *Cancer Genetics and Cytogenetics* **180**:100–109. DOI: <https://doi.org/10.1016/j.cancergencyto.2007.10.010>, PMID: 18206534

- Zbar B**, Alvord WG, Glenn G, Turner M, Pavlovich CP, Schmidt L, Hewitt SM. 2002. Risk of renal and colonic neoplasms and spontaneous pneumothorax in the Birt-Hogg-Dube syndrome. *Cancer Epidemiology and Prevention Biomarkers* **11**:393–400.
- Zhang D**, Iyer LM, He F, Aravind L. 2012. Discovery of novel DENN proteins: implications for the evolution of eukaryotic intracellular membrane structures and human disease. *Frontiers in Genetics* **3**:283. DOI: <https://doi.org/10.3389/fgene.2012.00283>, PMID: 23248642

Appendix 1

Appendix 1—key resources table

Reagent type (species) or resource	Designation	Source or reference	Identifiers	Additional information
Gene (<i>Homo sapiens</i>)	FLCN	HUGO Gene Nomenclature Committee	HGNC:27310	
Gene (<i>Homo sapiens</i>)	FNIP1	HUGO Gene Nomenclature Committee	HGNC:29418	
Gene (<i>Homo sapiens</i>)	FNIP2	HUGO Gene Nomenclature Committee	HGNC:29280	
Gene (<i>Homo sapiens</i>)	TFE3	HUGO Gene Nomenclature Committee	HGNC:11752	
Gene (<i>Homo sapiens</i>)	TFEB	HUGO Gene Nomenclature Committee	HGNC:11753	
Gene (<i>Homo sapiens</i>)	STAT1	HUGO Gene Nomenclature Committee	HGNC:11362	
Gene (<i>Homo sapiens</i>)	STAT2	HUGO Gene Nomenclature Committee	HGNC:11363	
Cell line (<i>Homo sapiens</i>)	RPE-1 tet on Cas9 TP53 ^{KO}	Benedict et al., 2020	PMID: 32084359	Originally derived from hTERT RPE-1 (ATCC Cat# CRL-4000, RRID: CVCL_4388)
Cell line (<i>Homo sapiens</i>)	RPE tet on Cas9 TP53 ^{KO} FLCN ^{KO} C2	This paper		knock out cell lines, see Material and methods section CRISPR/Cas9 gene editing
Cell line (<i>Homo sapiens</i>)	RPTEC/TERT1	ATCC	ATCC Cat# CRL-4031, RRID: CVCL_K278	
Cell line (<i>Homo sapiens</i>)	- RPTEC tet on Cas9 - RPTEC tet on Cas9 TP53 ^{KO} (pool and three clones) - RPTEC tet on Cas9 TP53 ^{KO} FLCN ^{KO} C1-3 - RPTEC RPTEC tet on Cas9 TP53 ^{wt} FLCN ^{KO} - RPTEC tet on Cas9 FNIP1/ FNIP2 ^{KO} - RPTEC FLCN ^{KO}	This paper		knock out cell lines, see Material and methods section CRISPR/Cas9 gene editing
Cell line (<i>Homo sapiens</i>)	- RPTEC SFPO-TFE3 - RPTEC SFPO-TFE3 FLCN ^{KO}	This paper		Lentivirally transduced SFPO-TFE3 mutant, with and without CRISPR mediated FLCN knock out
Sequenced-based reagent (human)	siRNA STAT1	Dharmacon, Horizon discovery	L-003543-00-0005	siRNA pool used for gene knock down experiments

Continued on next page

Appendix 1—key resources table continued

Reagent type (species) or resource	Designation	Source or reference	Identifiers	Additional information
Sequenced-based reagent (human)	siRNA STAT2	Dharmacon, Horizon discovery	L-012064-00-0005	siRNA pool used for gene knock down experiments
Sequenced-based reagent (human)	siRNA TFEB	Dharmacon, Horizon discovery	L-009798-00-0005	siRNA pool used for gene knock down experiments
Sequenced-based reagent (human)	siRNA TFE3	Dharmacon, Horizon discovery	L-009363-00-0005	siRNA pool used for gene knock down experiments
Sequenced-based reagent (human)	siRNA non-targeting control	Dharmacon, Horizon discovery	D-001210-04-05	siRNA pool used for gene knock down experiments
Transfected construct (human)	pLenti CMVie-IRES-BlastR FLCN cDNA	This paper		FLCN rescue by overexpression of cDNA in Addgene plasmid #119863 (<i>Puleo et al., 2019</i>)
Transfected construct (human)	pLKO-Ubc SFPO-TFE3	<i>Fumagalli et al., 2017</i>	PMID:28270604	Patient derived SFPO-TFE3 fusion sequence transduced in RPTEC
Sequenced-based reagent (<i>Homo sapiens</i>)	crRNA FLCN_exon 5 (GTGGC TGACGTATTTAA TGG)	Dharmacon, Horizon Discovery		Synthetic gRNA for CRISPR/Cas9 mediated gene knock out
Sequenced-based reagent (<i>Homo sapiens</i>)	crRNA FLCN_exon 7 (TGTCAGCGA TGTCAGCGAGC)	Dharmacon, Horizon Discovery		Synthetic gRNA for CRISPR/Cas9 mediated gene knock out
Sequenced-based reagent (<i>Homo sapiens</i>)	crRNATP53_exon 4 (CCATTGTTCAA TATCGTCCG)	Dharmacon, Horizon Discovery		Synthetic gRNA for CRISPR/Cas9 mediated gene knock out
Sequenced-based reagent (<i>Homo sapiens</i>)	crRNA FNIP1_exon 2 (GATATACAA TCAGTCGAATC)	Dharmacon, Horizon Discovery		Synthetic gRNA for CRISPR/Cas9 mediated gene knock out
Sequenced-based reagent (<i>Homo sapiens</i>)	crRNA FNIP2_exon 3 (GATGGTTG TACCTGGTAC TT)	Dharmacon, Horizon Discovery		Synthetic gRNA for CRISPR/Cas9 mediated gene knock out
Sequenced-based reagent (<i>Homo sapiens</i>)	FLCN_exon 4 GAGAGCCACGA UGGCAUUCA + modified EZ scaffold	Synthego		Synthetic gRNA for CRISPR/Cas9 mediated gene knock out
Biological sample (<i>Homo sapiens</i>)	BHD kidney tumor 1	This paper		BHD T1 sample for mass spectrometry, see Material and methods section Patient material
Biological sample (<i>Homo sapiens</i>)	BHD kidney tumor 2	This paper		BHD T2 sample for mass spectrometry, see Material and methods section Patient material
Biological sample (<i>Homo sapiens</i>)	Human kidney lysate 1	Novus Bio	NB820-59231	HK1 sample for mass spectrometry
Biological sample (<i>Homo sapiens</i>)	Human kidney lysate 2	Santa Cruz	sc-363764	HK2 sample for mass spectrometry

Continued on next page

Appendix 1—key resources table continued

Reagent type (species) or resource	Designation	Source or reference	Identifiers	Additional information
Antibodies (for westerns)	Vinculin (mouse mAb, H-10)	Santa Cruz	sc-25336	(1:1000)
	FLCN (rabbit mAb, D14G9)	Cell Signalling	CST 3697S	(1:1000)
	Cas9 (mouse mAb, 7A9)	Epigentek	A-9000–050	(1:1000)
	AQP1 (mouse mAb, B11)	Santa Cruz	sc-25287	(1:100)
	GPNMB (goat pAb)	R and D systems	AF2550-SP	(0.5 µg/mL)
	SQSTM1 (mouse mAb, D5L7G)	Cell Signalling	CST 88588	(1:1000)
	RRAGD (rabbit pAb)	Cell Signalling	CST 4470S	(1:1000)
	FNIP1 (rabbit mAb)	Abcam	ab134969	(1:1000)
	FNIP2 (rabbit pAb)	Atlas Antibodies	HPA042779	(1:1000)
	STAT2 (rabbit pAb)	GeneTex	GTX103117	(1:1000)
	pSTAT1 Y701 (rabbit mAb, D4A7)	Cell Signalling	CST 7649S	(1:1000)
	TFE3 (rabbit pAb)	Atlas Antibodies	HPA023881	(1:1000)
	H3 (rabbit pAb)	Cell Signalling	CST 9715S	(1:1000)
	αTubulin (mouse mAb, B-5-1-2)	Santa Cruz	sc-23948	(1:2000)
	p70S6Kinase T389 (rabbit pAb)	Cell Signalling	CST 9205	(1:1000)
	pAKT S473 (rabbit mAb, D9E)	Cell Signalling	CST 4060	(1:2000)
	total p70S6K (rabbit mAb, 49D7)	Cell Signalling	CST 2708	(1:1000)
	panAKT (mouse mAb 40D4)	Cell Signalling	CST 2920	(1:2000)
	4E-BP1 (rabbit mAb 53H11)	Cell Signalling	CST 9644	(1:1000)
	GAPDH (mouse mAb, 0411)	Santa Cruz	sc-47724	(1:5000)
GAPDH (mouse mAb, 6C5)	Merck Millipore	MAB374	(1:200)	

Continued on next page

Appendix 1—key resources table continued

Reagent type (species) or resource	Designation	Source or reference	Identifiers	Additional information
Antibodies (for immunofluorescence)	mTOR (rabbit mAb, 7C10),	Cell Signalling	CST 2983	(1:300)
	Lamp2 (mouse mAb, H4B4)	Abcam	ab25631	(1:400)
	TFE3 (rabbit pAb)	Cell Signalling	CST 14779	(1:300)
Sequence-based reagent	qRT-PCR and sequencing primers	Sigma-Aldrich		Described in corresponding material and method sections
Commercial assay or kit	Lenti-X Tet-On 3G Inducible Expression System	Clontech, Takara Bio	631187	Creation of lentiviral constructs to generate Doxycycline inducible Cas9 cell line
Commercial assay or kit	High Pure RNA Isolation Kit	Roche	11828665001	RNA isolation kit for RNAseq and qRT-PCR analyses
Commercial assay or kit	iScript cDNA Synthesis Kit	Bio-Rad	170-8891	cDNA synthesis kit for qRT-PCR analyses
Commercial assay or kit	IFN- γ Flex Set CBA	BD Biosciences	560111	Flow cytometry based Cytometric bead array
Commercial assay or kit	VeriKine-HS Human IFN- α All Subtype ELISA kit	PBL assay science	41115	IFN- α Enzyme-Linked Immunosorbent Assay
Chemical compound, drug	Crystal Violet		1014080025	Stain clonogenicity using a (0,05% solution)
Software, algorithm	R/Rstudio			edgeR (Robinson et al., 2010) ggplot (Wickham, 2016)
Software, algorithm	Cytoscape	Shannon et al., 2003	PMID: 14597658	iRegulon BinGO ClusterOne v1.0 (Nepusz et al., 2012)
Software, algorithm	GSEA MSigDB	Subramanian et al., 2005 Liberzon et al., 2011	PMID: 16199517 PMID: 26771021	Gene set enrichment analyses
Software, algorithm	GraphPad Prism		RRID: SCR_002798	Rel. 8.2.2, plots and graph design
Software, algorithm	AxioVision SE64	Carl Zeiss	Rel. 4.9.1	Microscope camera software